J|A|C|S
JOURNAL OF THE AMERICAN CHEMICAL SOCIETY

Article
pubs.acs.org/JACS

Rational Design of Helical Nanotubes from Self-Assembly of Coiled-Coil Lock Washers

Chunfu Xu,[†] Rui Liu,[†] Anil K. Mehta,[†] Ricardo C. Guerrero-Ferreira,[‡] Elizabeth R. Wright,[‡] Stanislaw Dunin-Horkawicz,[§] Kyle Morris,[∥,$] Louise C. Serpell,[∥] Xiaobing Zuo,[⊥] Joseph S. Wall,[¶] and Vincent P. Conticello*[,†]

[†]Department of Chemistry, Emory University, 1515 Dickey Drive, Atlanta, Georgia 30322, United States

[‡]Division of Pediatric Infectious Diseases, Department of Pediatrics, Emory University School of Medicine, Children's Healthcare of Atlanta, 2015 Uppergate Drive, Suite 500, Atlanta, Georgia 30322, United States

[§]Laboratory of Bioinformatics and Protein Engineering, International Institute of Molecular and Cell Biology, 4 Ks. Trojdena Street, Warsaw 02-109, Poland

[∥]School of Life Sciences, University of Sussex, Lewes Road, Falmer, East Sussex BN1 9QG, United Kingdom

[⊥]X-ray Science Division, Argonne National Laboratory, 9700 South Cass Avenue, Argonne, Illinois 60439, United States

[¶]Brookhaven National Laboratory, P.O. Box 5000, Upton, New York 11973, United States

Supporting Information

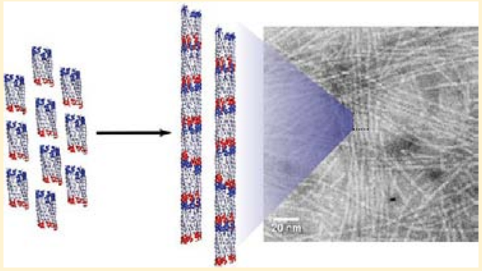

ABSTRACT: Design of a structurally defined helical assembly is described that involves recoding of the amino acid sequence of peptide **GCN4-pAA**. In solution and the crystalline state, **GCN4-pAA** adopts a 7-helix bundle structure that resembles a supramolecular lock washer. Structurally informed mutagenesis of the sequence of **GCN4-pAA** afforded peptide **7HSAP1**, which undergoes self-association into a nanotube via noncovalent interactions between complementary interfaces of the coiled-coil lock-washer structures. Biophysical measurements conducted in solution and the solid state over multiple length scales of structural hierarchy are consistent with self-assembly of nanotube structures derived from 7-helix bundle subunits. The dimensions of the supramolecular assemblies are similar to those observed in the crystal structure of **GCN4-pAA**. Fluorescence studies of the interaction of **7HSAP1** with the solvatochromic fluorophore PRODAN indicated that the nanotubes could encapsulate shape-appropriate small molecules with high binding affinity.

INTRODUCTION

Structurally defined materials on the nanometer length scale have been historically the most challenging to rationally construct and the most difficult to structurally analyze.[1,2] Sequence-defined polypeptides represent attractive design elements for construction of these types of nanoscale materials. Sequence−structure correlations from native proteins can be employed for design of ordered assemblies in which functional properties can be controlled through the progression of structural hierarchy encoded at the molecular level. Furthermore, proteins are amenable to preparative-scale synthesis and display a rich portfolio of structure and function in the native state. However, the diversity of sequence space and current limitations of theoretical approaches to reliably define the relationship between sequence and supramolecular structure present a significant challenge to the de novo design of novel materials architectures.

Simple protein motifs, such as α-helical coiled coils,[3−9] β strands,[10−15] β hairpins,[16,17] and collagen triple helices,[18−25] have been employed as structural elements for the de novo design of fibrillar protein-based assemblies with a notable degree of success. Thus far, however, it has proven difficult to reliably predict higher order structure and almost impossible to specify function to a similar extent as observed for native protein assemblies. This phenomenon may be attributed, at least in part, to differences in the self-assembly mechanism between synthetic and native protein assemblies. For the synthetic systems, self-assembly usually occurs commensurately with folding of the peptide sequence into the target structure. This strategy requires the ability to define structure simultaneously over multiple length scales. In contrast, the structural subunits of native protein fibrils usually comprise folded protein domains or structurally defined oligomeric assemblies that self-associate through the recognition between structurally complementary interfaces, usually reversibly and controllably, in response to environmental cues.

An alternative strategy for creation of synthetic protein assemblies may be envisioned that hews more closely to the native mechanism of self-assembly.[26] Since the structures of

Received: July 19, 2013
Published: September 11, 2013

dx.doi.org/10.1021/ja4074529 | *J. Am. Chem. Soc.* 2013, 135, 15565−15578

folded protein domains can be determined to high resolution using single-crystal X-ray diffraction or multidimensional NMR spectroscopic analyses, one can potentially introduce structurally informed mutations at surface-exposed positions within these sequences to promote specific modes of self-association that would permit retention of native function and/or creation of novel function within the self-assembled material. We employ this recoding strategy to redesign the sequence of the peptide **GCN4-pAA**[27] to promote specific recognition between interfaces such that linear propagation occurs to form uniaxially oriented tubular assemblies.[28,29]

The crystal structure of **GCN4-pAA** (PDB ID 2HY6), a de novo designed peptide derived from the leucine zipper region of the *S. cerevisiae* transcription factor GCN4,[30] displays a discrete 7-helix bundle structure that comprises the largest, freely standing coiled-coil oligomer that has been structurally characterized thus far (Figure 1). The heptameric assembly defines a continuous central channel with an internal diameter of approximately 7 Å.[27] Computational analysis using the program CASTp[31] indicated the presence of an internal void volume of 1880 Å^3 associated with the central channel. The presence of several hexane-1,6-diol molecules in the central channel of the heptamer crystal structure indicates that it is capable of accommodating appropriately shaped small molecules within the cavity. In addition, the **GCN4-pAA** bundle structure displays a single-residue shift in registry between adjacent helices, which resulted in an overall displacement of seven residues (i.e., one coiled-coil heptad) at the interface between helices *A* and *G* of the bundle structure (Figure 1). The 7-helix bundle of **GCN4-pAA** resembles a lock washer in which the displaced edges at the interface between helices *A* and *G* provide additional surface area for complementary interactions between the coiled-coil protomers. In contrast, most coiled-coil structures do not display a commensurate shift in helix registry.

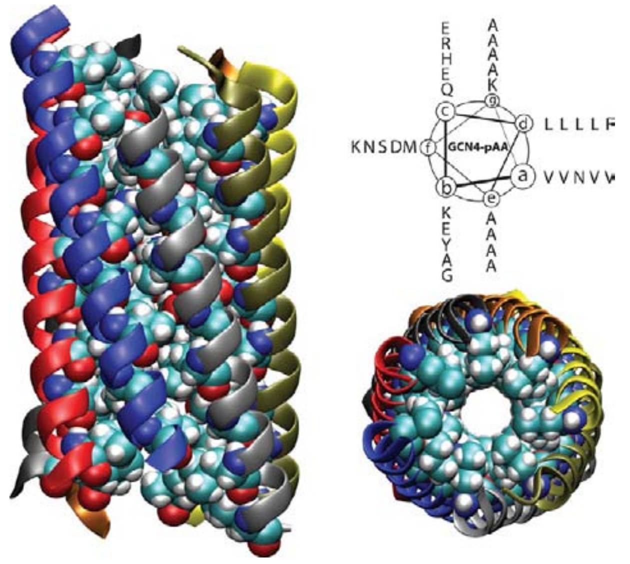

Figure 1. Crystal structure (PDB ID 2HY6) of the 7-helix bundle resulting from self-association of the peptide **GCN4-pAA**. Full-length and top-down views are shown on the left and in the lower right, highlighting side-chain atoms of residues pointing toward the tube interior. Individual helices (*A*−*G*) are colored separately. Displaced edge of the structure occurs at the interface between the first (*A*, blue) and the seventh (*G*, gray) helices. Helical wheel projection of the amino acid sequence of **GCN4-pAA** in 7_2-supercoil helix space (upper right).

The program MSMS[32] was employed to calculate the solvent-accessible surface area (SASA) associated with the exposed edges at the *N*-terminal and *C*-terminal surfaces of the **GCN4-pAA** 7-helix bundle. SASA values of 2411 and 1310 Å^2 were determined for the upper (*N*-terminal) surface and exposed edge of helix *A* and for the lower (*C*-terminal) surface and exposed edge of helix *G*, respectively. The SASA differences between the upper and the lower surfaces may be attributed to differences in amino acid composition and are, therefore, amenable to modification. The surface area that would be buried through formation of a helical interface between stacked bundles was estimated by comparison to the remnant solvent-accessible surface area calculated for structurally homologous positions at internal sites within the structure of **GCN4-pAA** (see Methods). Subtracting these values from the total SASA of the exposed upper and lower interfaces of **GCN4-pAA** one would expect approximately 1100−1200 and 900 Å^2 of surface area, respectively, to be buried upon self-association between structurally complementary surfaces of 7-helix bundles. Bennett et al.[33] proposed a minimum interaction surface area of 856 Å^2 per interface for formation of stable fibrillar assemblies, based on structural analysis of interfaces in protein crystals postulated by Ponstingl et al.[34] The interfaces of **GCN4-pAA** seem more than sufficient to meet the minimal criteria for formation of stable end-to-end association; a necessary prerequisite for formation of structurally defined assemblies.

Despite these observations, heptameric coiled-coil assemblies of **GCN4-pAA** do not appear to interact significantly in solution or the crystalline state.[27] No axial interactions were observed between 7-helix bundles at cutoff distances ≤ 9.0 Å in the crystal structure of **GCN4-pAA**. This distance is equivalent to the axial rise of six amino acid residues within an α-helical conformation, which implies that a significant gap exists between coaxially oriented 7-helix bundles in the crystal structure of **GCN4-pAA**. Moreover, sedimentation equilibrium analytical ultracentrifugation of solutions of **GCN4-pAA** indicated clean formation of a heptamer within the experimentally measured concentration range (30−300 μM) in ABS buffer (50 mM acetate, pH 5.2, 150 mM NaCl) at 20 °C.[27]

Several features of the **GCN4-pAA** sequence may act to frustrate interfacial interactions between helical bundles and, therefore, may be subject to improvement through rational design. Notably, an arginine residue occurs at a *d* position within the *C*-terminal heptad of **GCN4-pAA** (Figure 1), which breaks the hydrophobic periodicity of the repeat sequence. Charged gatekeeper residues at protein−protein interfaces have been demonstrated to act as negative design elements that prevent self-association in β-sheet proteins.[35] Similarly, the positive charge of the arginine residue should have a direct influence on the Coulombic attraction between the uncapped *N*- and *C*-termini of **GCN4-pAA**. Thus, disruption of the hydrophobic core and introduction of repulsive interfacial interactions would be expected to inhibit self-association between heptameric assemblies derived from **GCN4-pAA**. We hypothesized that if the sequence of **GCN4-pAA** was modified to remove these inhibitory structural features then end-to-end association should occur between complementary surfaces of the lock-washer structures that would result in formation of a high aspect ratio fibril with a continuous channel throughout the assembly.

■ RESULTS AND DISCUSSION

Peptide **7HSAP1** was designed to test the hypothesis described above (Figure 2). Design of **7HSAP1** reflects several critical structural considerations. The thermodynamic driving force for self-assembly of the nanotubes should be a combination of electrostatic attraction between the oppositely charged surfaces and burial of solvent-accessible surface area at structurally complementary interfaces between lock-washer subunits (i.e., 7-helix bundles). The hydrophobic *a*–*d*–*e*–*g* interface[27] of the original **GCN4-pAA** peptide was maintained as it was reasoned that this feature was necessary to ensure formation of the seven-helix bundle. However, the single arginine residue at a *d* position within the sequence of **GCN4-pAA** was replaced with a canonical leucine residue in order to maintain a continuous hydrophobic interface and remove repulsive electrostatic interactions that might arise between bundles. The *N*- and *C*-termini of the peptide were left uncapped to promote head-to-tail stacking interactions through electrostatic attraction between oppositely charged interfaces of the lock-washer structures. In addition, electrostatic interactions were maximized between the spatially proximal *b* and *c* positions on adjacent helices (Figure 2) with glutamate and lysine, respectively, in order to strengthen association between individual helices within the 7-helix bundle. The peptide sequence was formally split between the *b* and the *c* positions of the heptad repeat in order to minimally perturb the *a*–*d*–*e*–*g* hydrophobic core. To preserve continuity of the coiled-coil structural periodicity upon axial stacking of the lock-washer assemblies, the sequence of **7HSAP1** was based on an integral number of five heptad repeats. Finally, two arginine residues were placed at *f* positions within the **7HSAP1** sequence. The resultant positive charge of (+2) per peptide should hinder lateral association between bundles and promote dispersion of the assemblies in solution.

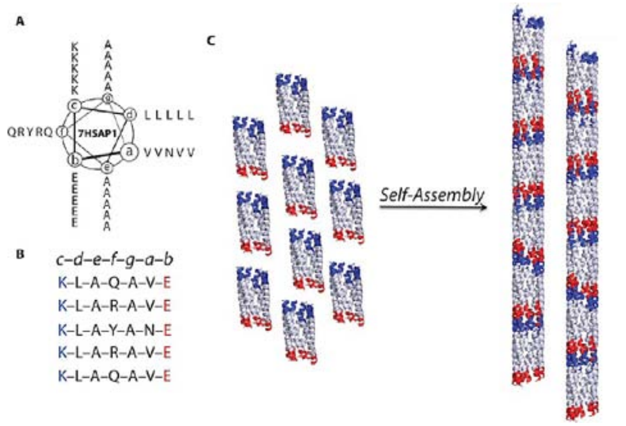

Figure 2. (Left) Helical wheel (A) and linear depiction (B) of the sequence of peptide **7HSAP1**. (Right) Schematic representation of the proposed model for self-assembly (C) of lock-washer structures derived from the 7-helix bundle of peptide **7HSAP1** into helical nanotubes. Blue and red surfaces represent the positively charged (*N*-terminal) heptads and negatively charged (*C*-terminal) heptads at the interfaces between 7-helix bundle subunits of **7HSAP1** assemblies.

A range of analytical methods was employed to evaluate the structure of **7HSAP1** over multiple length scales in solution and the solid state. The conformation of **7HSAP1** peptide was initially interrogated with circular dichroism (CD) spectropolarimetry. The CD signal is strongly α-helical with MRE values that exceed those of the control peptide **GCN4-pAA**[27] under identical conditions of buffer concentration and pH (100 μM peptide in 10 mM MES buffer pH 6.0) and approach 100% helicity (Figure 3). Under these conditions, peptide **7HSAP1** did not display a melting transition between 4 and 95 °C, which is consistent with the presence of an extended hydrophobic core and commensurate with earlier CD melting studies of **GCN4-pAA** under similar conditions (Supporting Information, Figure S4).

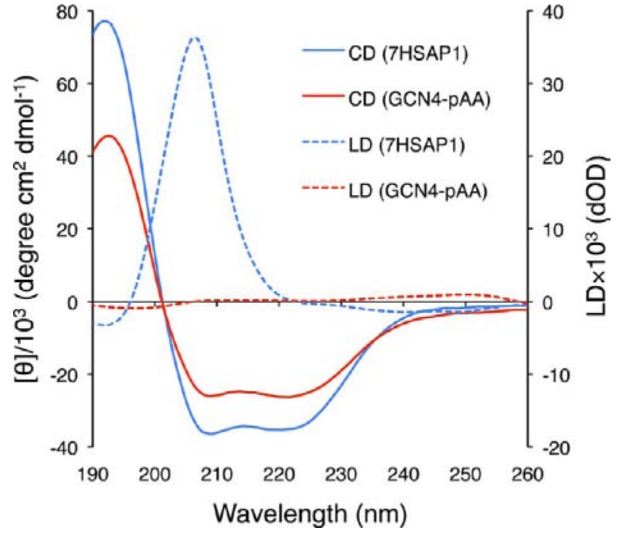

Figure 3. Circular dichroism and flow linear dichroism spectra of peptides **GCN4-pAA** and **7HSAP1** (100 μM) in 10 mM MES buffer, pH 6.0. Flow linear dichroism spectra were acquired under a Couette flow of 3000 rpm.

Flow linear dichroism[36] was employed under conditions of similar concentration to assess the degree of anisotropy that developed within the peptide samples under a flow alignment (3000 rpm) in a Couette cell (Figure 3). Solutions of **7HSAP1** displayed an LD spectrum with a strong positive signal at 207 nm, which provides evidence that the amide bond chromophores are aligned in parallel to the flow direction and therefore along the long axis of the assembly. In addition, the negative feature at 190 nm would also be expected for a helix oriented in the direction of flow, since it arises from a transition perpendicular to the helical axis. Similar LD spectroscopic results have been observed for solutions of a synthetic coiled-coil fiber and the dimeric coiled-coil protein tropomyosin that had been aligned under Couette flow.[37]

LD and CD results are consistent with the hypothesis that **7HSAP1** assembles in solution as an α-helical bundle to form extended arrays that stack along the direction of the superhelical axis (Figure 2). In contrast, solutions of **GCN4-pAA** did not display a flow LD spectrum that differed significantly from the baseline (Figure 3). This observation suggests that solutions of **GCN4-pAA** could not be aligned in the Couette cell, presumably as a consequence of their inability to form stable, extended arrays. Changes in solution conditions, such as lowered pH (50 mM acetate, pH 5.2) or addition of cosolvents (0.1% dimethylformamide), resulted in loss of the flow LD signal of **7HSAP1**. These LD results suggest that self-association between the structurally complementary interfaces of **7HSAP1** were subject to disruption under shear flow, even though the CD spectroscopic signature and fibrillar morphol-

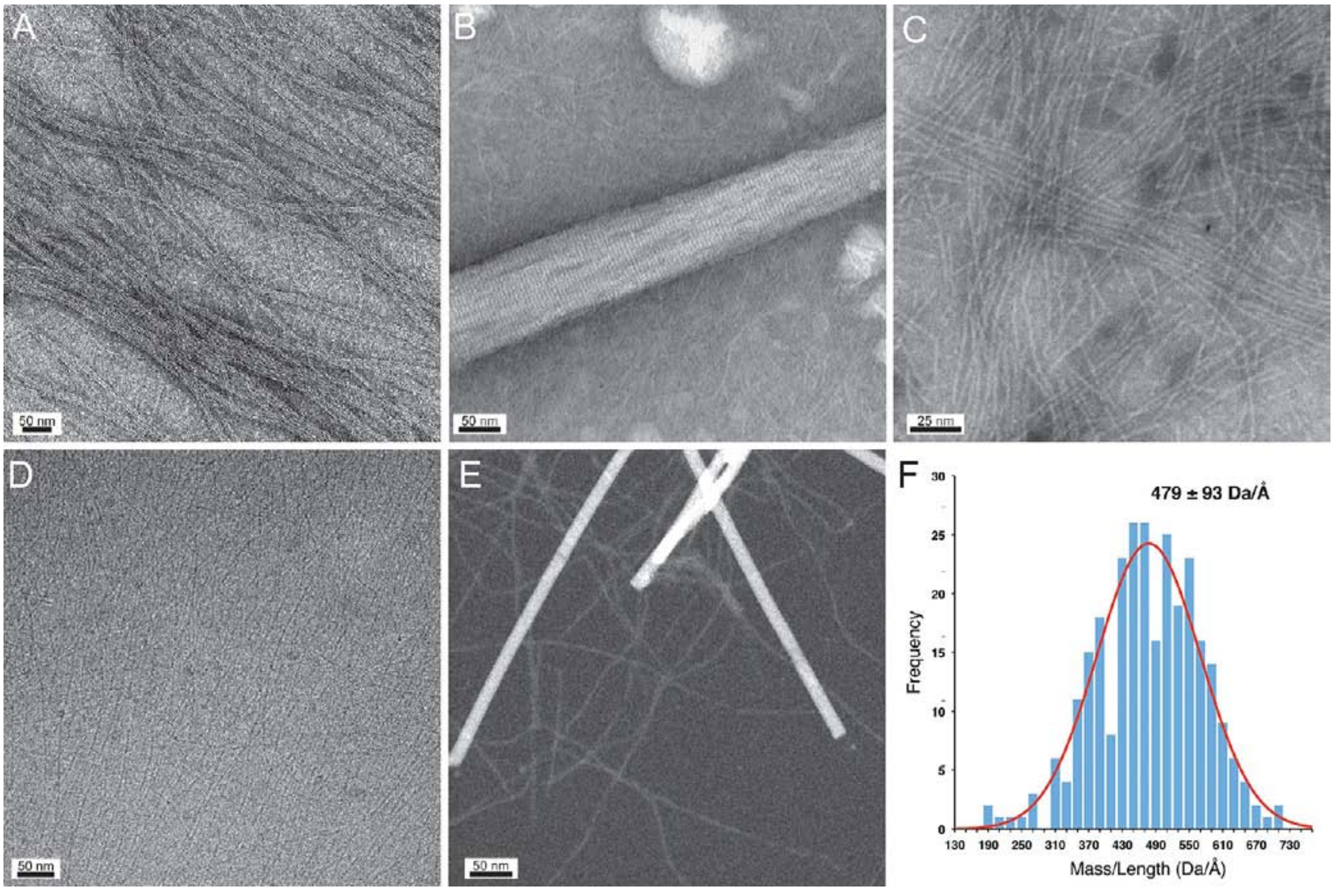

Figure 4. Electron microscopy analysis of **7HSAP1** assemblies. (A) Conventional TEM of **7HSAP1** (2.2 mM) in MES buffer (10 mM, pH 6.0) stained with 2% mixture of 1:1 methylamine vanadate and methylamine tungstate. (B) Conventional TEM of large paracrystalline assemblies derived from **7HSAP1** (2 mM) in MES buffer (10 mM, pH 6.0) stained with 1% uranyl acetate. (C) STEM of **7HSAP1** (80 μM) in MES buffer (10 mM, pH 6.0) stained with 2% methylamine vanadate. (D) Cryo-TEM of **7HSAP1** (130 μM) in MES buffer (10 mM, pH 6.0). (E) Dark-field STEM of freeze-dried, unstained specimens of **7HSAP1** assemblies (8 μM). Larger assemblies correspond to the TMV calibrant. (F) Histogram of mass per unit length (MPL) measurements of the **7HSAP1** specimen (after normalization to the TMV standard).

ogy (vide infra) were not perturbed under identical static conditions. The malleable nature of the interactions between subunits is consistent with the action of noncovalent forces (i.e., electrostatic, van der Waals, and hydrogen-bonding interactions), the strength of which can be manipulated through changes in environmental conditions.

TEM analysis (Figure 4A) of **7HSAP1** in MES buffer (10 mM, pH 6.0) confirmed formation of fibrillar structures over a wide range of peptide concentration (at least 25 μM to 4.0 mM). Under conditions of conventional TEM analysis, fibrils were observed to bundle together, occasionally affording highly ordered paracrystalline assemblies (Figure 4B and Figure S5, Supporting Information) at higher concentrations ($\geq$2 mM). In contrast, fibrillar structures were not observed in the TEM analysis of solutions of peptide **GCN4-pAA**, even at the higher concentration limit. Capping of **7HSAP1** as the *N*-acetyl and *C*-amide derivative significantly inhibits but does not abolish fibrillization of the peptide, as observed for other coiled-coil fibrils.[4] This observation suggests that **7HSAP1** has a stronger intrinsic propensity for self-assembly than **GCN4-pAA**, which may result from introduction of energetically stabilizing interactions and removal of destabilizing interactions in the initial peptide design (vide supra).

Cryo-TEM (Figure 4D) of solutions of **7HSAP1** (130 μM in 10 mM MES buffer, pH 6.0) indicated the presence of fibrils of ca. 3 nm in diameter. STEM analysis of negatively stained specimens of **7HSAP1** (80 μM) confirmed the fibril diameter (3.0 ± 0.1 nm). A lesser population ($\leq$10%) of thinner fibrils was observed with a diameter of ca. 2.0 nm. The observed diameter of the major population of **7HSAP1** fibrils compared well with the diameter of 3.1 nm observed for the 7-helix bundle in the crystal structure of **GCN4-pAA.**[27] In addition, the lateral striations in the negatively stained, paracrystalline assemblies of **7HSAP1** were determined to have a spacing of approximately 5 nm (Figure 4B). This distance coincides with the length of the **7HSAP1** peptide projected onto the superhelical structural parameters determined from the 7-helix bundle structure of **GCN4-pAA** (superhelical rise/residue of 0.143 nm × 35 residues = 5.01 nm).[27] Similar striations have been observed in the TEM analysis of negatively stained fibrils derived from self-assembly of coiled-coil dimers.[4d,e] The lateral spacings in these cases were also determined to coincide with the length of the peptide projected onto the corresponding dimeric coiled-coil structure.[4d,e]

While the combined data suggested that the major structural feature was fibrils derived from self-assembly of 7-helix bundle structures, STEM measurements indicated a smaller population of thinner fibrils ($\leq$10%) within the specimens assembled at the lower concentration conditions ($\leq$100 μM) employed for imaging (Figure 4E). Mass action effects could tilt the

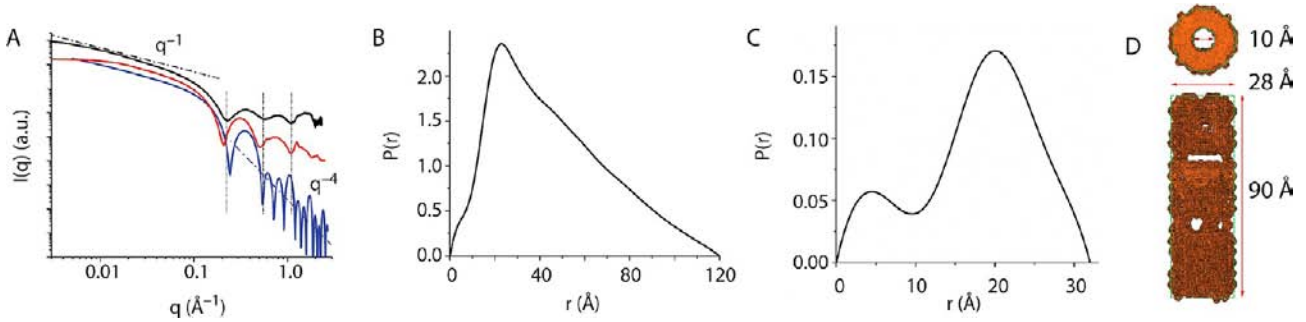

Figure 5. (A) Experimental SAXS/WAXS scattering profile (black curve) for **7HSAP1** (1 mM) in MES buffer (10 mM, pH 6.0) along with simulated data for a hollow cylindrical model (blue curve) and a molecular model (red curve) based on five stacked seven-helix bundles of **7HSAP1**. (B) Pair distance distribution function (PDDF) of **7HSAP1**, calculated from the SAXS ($I(q)$ versus q) data using program GNOM.[40] (C) Cross-section PDDF calculated from SAXS data ($qI(q)$ versus q) using GNOM. (D) Top and side views of the SAXS molecular envelope derived from a nanotube search space with R_{in} of 5 Å and R_{out} of 14 Å using scattering data from **7HSAP1** and the program DAMMIN.[42] Scattering data within the q range of 0.03−0.58 Å^{-1} were used in calculations of B, C, and D. Largest molecular dimension (r_{max} in B) and length of the SAXS molecular envelope may be underestimated due to the limited available low q data.

equilibrium toward fibril disassembly under these circumstances. In support of this hypothesis, STEM measurements provide evidence of breaks within the filaments at the more dilute concentration range (<80 μM), which was consistent with this hypothesis. In addition, solid-state ^{13}C CP/MAS NMR spectroscopy of fibers derived from the isotopically labeled peptide variant **7HSAP1*** (vide infra) indicated the absence of β-sheet conformation even under conditions of assembly at high peptide concentration (Figure S7, Supporting Information). These results argued against the formation of amyloid fibrils as a side product of peptide self-assembly.

Cryo-STEM. Mass per length (MPL) measurements were performed on **7HSAP1** filaments (8 μM in 10 mM MES buffer pH 6.0) imaged using dark-field STEM of unstained, freeze-dried specimens (Figure 4E). Tobacco mosaic virus (TMV) particles were employed as an internal mass standard. The majority of the specimen corresponded to filaments of approximately 3 nm in diameter, as observed previously. A MPL value of 479 ± 93 Da/Å was determined for the 3 nm filaments, after normalization based on MPL measurements of the TMV mass standard (Figure 4F). A smaller population (ca. 10% of the specimen) corresponded to thinner filaments with approximately one-half of the MPL of the major component. A relatively large error (±19%) was observed on the MPL measurements in comparison to the values usually obtained (circa ±9%) in measurements of similar peptide and protein filaments.[38]

The observed MPL of the **7HSAP1** fibrils can be compared to that calculated for nanotube assemblies derived from stacking of 7-helix bundles analogous to that of **GCN4-pAA**. We used the crystal structure of **GCN4-pAA** to generate a model for the **7HSAP1** fibril (vide infra), in which a bundle length of ca. 52 Å was calculated based on the superhelical rise/residue of 1.45 Å and an average spacing between bundles of 1.6 Å. Using this value and the molar mass of **7HSAP1** (3823 Da), a MPL value of 511 Da/Å was calculated for a stacked assembly of 7-helix bundles. This value is within experimental error of the MPL value observed from dark-field STEM measurements. However, due to the large variance in the MPL measurements, a filament based on a 6-helix bundle structure could not be ruled out as the structural subunit. Design and structural characterization of individual (i.e., nonfibrillar) 6-helix bundles based on coiled-coil motifs has been described recently.[39] However, the 6-helix bundles differ significantly in core sequence from those of **7HSAP1** and **GCN4-pAA** and form in-register cylinders rather than edge-displaced lock-washer structures.

Solution X-ray Scattering Measurements. Small- and wide-angle X-ray scattering (SAXS/WAXS) data were collected on aqueous solutions of **7HSAP1** in MES buffer (10 mM, pH 6.0) to interrogate the structural hierarchy of the resultant assemblies at length scales over two decades. The small-angle range, i.e., the scattering momentum transfer (q), less than 0.2 Å^{-1} reflects the global shape of the molecule, while the middle q range, ca. $0.2 < q < 1.1$ Å^{-1}, reflects the tertiary fold of the assembly.

In the small-angle region, the experimental scattering intensities at $q < 0.1$ Å^{-1} roughly follow the q^{-1} power law (Figure 5A), indicating the assembly in solution has rod- or cylinder-like form. The pair distance distribution function (PDDF)[40] in Figure 5B derived from the SAXS data has a characteristic long tail, which further confirms the cylindrical shape. A cross-section PDDF derived from $qI(q)$ exhibits a bimodal form, indicating the cylindrical molecular assembly is hollow. The largest dimension of the cross-section is about 32 Å. The average wall thickness and diameter of the middle of the cylindrical shell can be estimated from the two maxima of the PDDF as ca. 10 and 20 Å, respectively, and the diameter of the hollow channel is about 10 Å. The value of R_c, the radius of gyration of the rod cross-section, was obtained as 12.4 Å through the fitting of the modified Guinier equation,[41] $I(q) = \pi q I(q = 0)\exp(-0.5R_c^2q^2)$. The discrepancy between the data and the rod-like q^{-1} power law at $q < 0.01$ Å^{-1} reflects the inhomogeneity of the assembly length in solution.

To further interpret the scattering data at higher angle regions, a molecular model was generated that corresponded to five stacked seven-helix bundles of **7HSAP1** (vide infra). Simulation of the X-ray scattering profile for this molecular model approximately reproduces the two scattering peaks centered at 0.35 and 0.80 Å^{-1} in the experimental data in terms of the peak and valley positions (Figure 5A). Simulations on the hollow cylindrical object model showed that the inner and outer radii determined the valley position (see Figure S6, Supporting Information). Therefore, the cross-section dimensions of the molecular model are very close to those in the sample. The more damped peak−valley ratio in the experimental data is partially due to higher thermal dynamics/disorder in the sample and the limitations inherent in the molecular model. At high angle, the scattering peak centered at 1.5 Å^{-1} arises from the repeatable occurrence of the atom pairs with 3−6 Å distances within the α helices, which were also partially reproduced in the simulated scattering for the molecular model.

The full-range scattering data could not be fit using a structural model based on a hollow cylindrical geometric object of uniform electron density. The impact of the electron density fluctuation within the molecule becomes significant at q values of ≥0.3 Å^{-1}, which influences the intensity and position of the peaks and valleys (Figure 5A). However, an ab initio three-dimensional envelope reconstruction from SAXS data was performed, and the derived SAXS molecular envelope exhibits a hollow cylindrical shape with inner and outer radii of ca. 5 and 14 Å, respectively. The SAXS envelope yields a R_c of 10.5 Å under the uniform electron density assumption where $R_c = (R_{in}^2 + R_{out}^2/2)^{1/2}$. The R_c value of the envelope agrees fairly well with the previous R_c from the modified Guinier fitting, considering the density fluctuation in the SAXS envelope model. Taken together, the SAXS/WAXS data support the presence of hollow nanotube assemblies in solutions of **7HSAP1** with lateral dimensions that approximate those observed in the crystal structure of the 7-helix bundle of **GCN4-pAA** (R_{out} = 15.5 Å, R_{in} = 3.5 Å).

X-ray Fiber Diffraction. X-ray fiber diffraction data collected from air-dried, partially aligned bundles of fibers (Figure 6) show a sharp signal on the meridian at 10.1 Å as well as weaker, more diffuse reflections at 5.1 and 4.3 Å. On the equator, reflections appear at around 26, 14.5 Å and 8 Å. The meridional reflections observed at 5.1 and 10.1 Å are consistent with the regular repeat that arises from α helices, and the position on the meridian supports the view that the α helices are aligned parallel to the fiber axis, which is consistent with the flow LD spectral data in solution. Analyses of the equatorial spacings are commensurate with a unit cell of similar dimensions to the diameter of the model structure (30 Å). An X-ray fiber diffraction pattern was calculated from structural coordinates of a molecular model corresponding to five stacked seven-helix bundles of **7HSAP1** (vide infra). The model was placed into a unit cell with hexagonal packing (a = 30 Å, b = 30 Å, c = 52 Å, $\alpha = \beta = 90°$, $\gamma = 120°$) using the program Clearer.[43] The calculated pattern is shown in comparison to the experimental diffraction data in Figure 6. Calculated signals match well with positions of signals in the experimental data. Discrepancies between relative intensity are observed, and this is likely to arise from differences in side-chain rotamers and minor backbone conformational differences. However, the results are supportive of the proposed model structure for assemblies of **7HSAP1** that correspond to stacked seven-helix bundle structures (Figure 2). Alternatively, 6-helix bundle structures[39] were examined as models; however, the 7-helix bundle structure afforded a better fit to the unit cell and was more consistent with the experimental fiber diffraction.

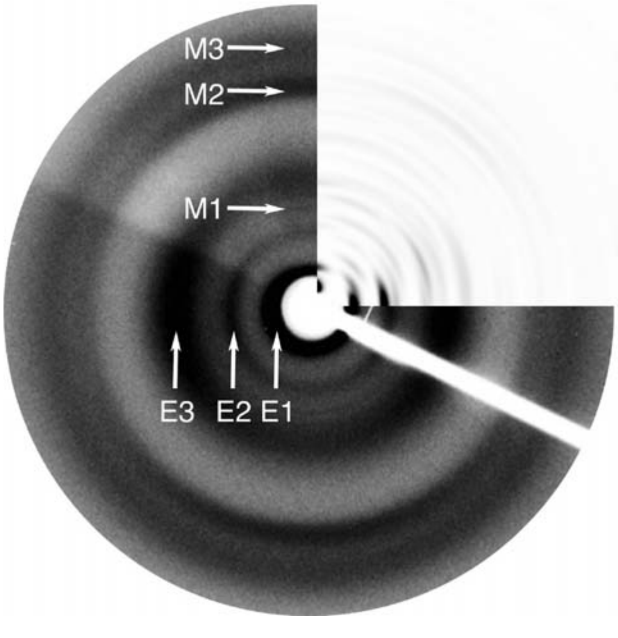

Figure 6. X-ray fiber diffraction of **7HSAP1** obtained from dried, partially oriented fibrillar assemblies. Equatorial reflections are noted at 26 (E1), 14.5 (E2), and 8 Å (E3), while meridional reflections are noted at 10.2 (M1), 5.1 (M2), and 4.3 Å (M3). Upper right quadrant corresponds to the calculated diffraction pattern of stacked 7-helix bundle assemblies of **7HSAP1** based on a unit cell with hexagonal packing (a = 30 Å, b = 30 Å, c = 52 Å, $\alpha = \beta = 90°$, $\gamma = 120°$). M1 reflection is too weak to observe in the simulation but can be detected through the off-meridionals that are part of that layer line.

Solid-State NMR Measurements. In order to obtain proof of the registry shift within the fibrillar assemblies of **7HSAP1**, we used distance measurements from solid-state NMR. A variant peptide, **7HSAP1***, was synthesized in which the Ala12 CO and Ala24 CH_3 groups were enriched with ^{13}C and the Leu16 NH group was enriched with ^{15}N. This labeling scheme, with a ca. 160 ppm chemical shift difference between ^{13}CO and $^{13}CH_3$ (Figure S7, Supporting Information), allows for independent determination of both the intramolecular backbone Ala12 ^{13}CO−Leu16 ^{15}N distance and the intermolecular Ala24 CH_3−Leu16 amide ^{15}N distance. The [1-^{13}C]Ala12−[3-$^{13}CH_3$]Ala24 intramolecular distance of ca. 17 Å minimizes any homonuclear ^{13}C−^{13}C dipolar coupling. The Ala12 ^{13}CO−Leu16 amide ^{15}N distance corresponds to an intramolecular *i,i+4* hydrogen-bonded pair of residues and can be correlated to the fraction of the **7HSAP1*** peptide that has folded into an α-helical conformation. The average intramolecular C−N distance between H-bonded *i,i+4* residues at homologous positions in the 7-helix bundle structure of **GCN4-pAA** is 4.1 Å (Figure 7E).[27] Distances on this length scale are straightforward to measure using $^{13}C\{^{15}N\}$REDOR and can be employed as an internal standard to calibrate more variable intermolecular distances within the 7-helix bundle.

The Ala24 CH_3−Leu16 amide ^{15}N distance corresponds to an intermolecular contact between adjacent helical interfaces within the 7-helix bundle structure. However, as solid-state NMR ^{13}C−^{15}N distance measurements are limited to less than 7 Å, this distance can only be determined at the interface between helices A and G of the suppositious 7-helix bundles of **7HSAP1** assemblies. Using the crystal structure of **GCN4-pAA** as a guide (Figure 7E),[27] the distance between labeled atoms at structurally homologous positions in **7HSAP1*** could be calculated. The intramolecular Ala24 $^{13}CH_3$−Leu16 amide ^{15}N distance in **7HSAP1** was determined to be ca. 13 Å, while the closest intermolecular distance between structurally adjacent helices within the 7-helix bundle is ca. 11 Å at the non-A/G helical interfaces. Both of these distances correspond to ^{13}C−^{15}N dipolar couplings that are too weak to be measured with solid-state NMR. However, the registry shift between adjacent helices places the Leu16 amide of helix G and the Ala24 CH_3 of helix A in close contact: 3.5 Å within the crystal

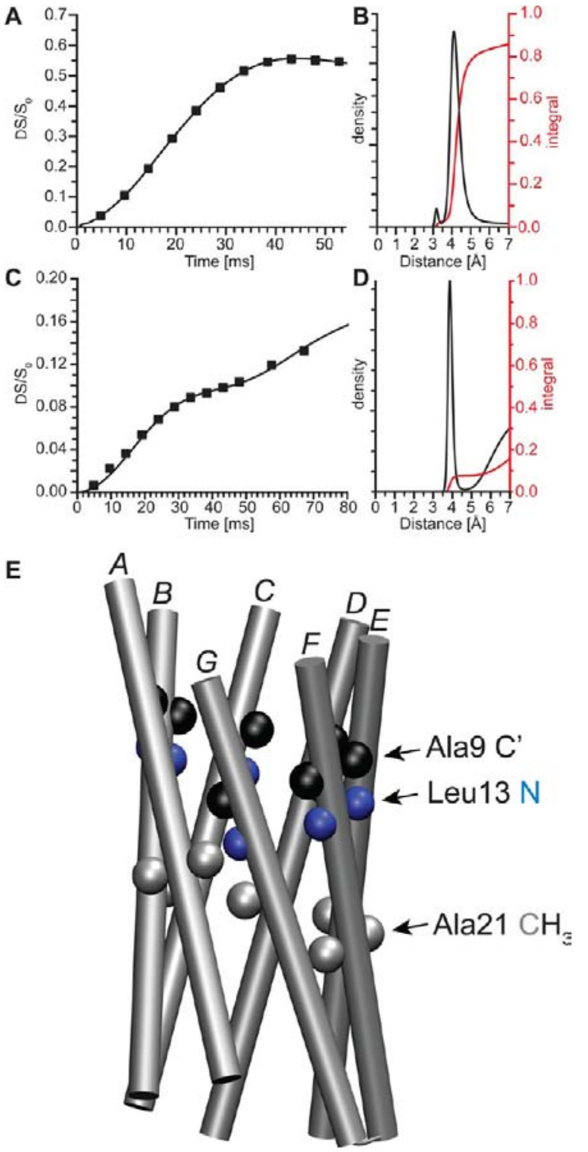

Figure 7. Solid-state NMR $^{13}C-^{15}N$ distance measurements of nanotubes derived from self-assembly of **7HSAP1*** peptides. (A) $^{13}C\{^{15}N\}$REDOR dephasing for [1-^{13}C]A12 [^{15}N]L16-**7HSAP** (**7HSAP***). Solid line is the calculated best-fit REDOR curve with distances from BS-REDOR fits (B) to experimental data. BS-REDOR best fit has ca. 85% (red curve) of Ala12 ^{13}CO to Leu16 ^{15}N spin pairs centered at 4.1 Å (black curve), which is consistent with *i,i+4* hydrogen bonding. (C) $^{13}C\{^{15}N\}$REDOR dephasing for [3-^{13}C]A24 [^{15}N]L16-**7HSAP1**, and (D) distance distribution from BS-REDOR fit to experimental data with 8% of Ala24 $^{13}CH_3$ at 3.9 Å from Leu16 ^{15}N with a narrow distribution and a second ill-defined distribution with ca. 8% of $^{13}CH_3-^{15}N$ distances > 6 Å. (E) Diagram of the 7-helix bundle structure of **GCN4-pAA**[27] in which helices *A*−*G* are drawn as cylindrical rods. Colored spheres indicate atoms within the 7-helix bundle of **GCN4-pAA** that occupy structural homologous positions with respect to the isotopically labeled sites in **7HSAP1***: carbonyl carbons (C′) of Ala9 (black), amide nitrogens of Leu13 (blue), and methyl carbons of Ala21 (gray). Closest contact between AlaCH$_3$−LeuN corresponds to a distance of 3.5 Å at the displaced interface between helices *A* and *G*.

structure of **GCN4-pAA**. Since this intermolecular contact defines the displaced edge of the 7-helix bundle, the corresponding distance can be correlated with peptide registry within the assembly and retention of the screw symmetry observed in the parent **GCN4-pAA** system (Figure 7E).

The unbiased fit of the Ala12 ^{13}CO $^{13}C\{^{15}N\}$REDOR[44] dephasing data, using a Boltzmann maximum-entropy approach (BS-REDOR),[45] as isolated $^{13}C-^{15}N$ spin pairs (Figure 7A and B) indicates that 85% of Ala12 ^{13}CO are directly H bonded to Leu16 amide ^{15}NH with the remaining 15% of the Ala12 ^{13}CO having $^{13}C-^{15}N$ distances greater than 7 Å. This observation suggests that in the NMR sample preparation approximately 85% of the peptide is folded into an *α* helix. The ^{13}C CP/MAS NMR spectrum of **7HSAP1** (Figure S7, Supporting Information) did not exhibit a distinct upfield *β*-sheet resonance for the Ala12 ^{13}CO chemical shift, consistent with the hypothesis that 15% of the Ala12 ^{13}CO with no ^{15}N REDOR dephasing corresponded to peptide in a disordered conformation. The disordered fraction of the sample could result from denaturation during sample preparation and/or incomplete self-assembly. However, $^{13}C\{^{15}N\}$REDOR data suggest that the helical portion of the sample is structurally defined with a narrow distribution of $^{13}C-^{15}N$ distances centered at 4.1 Å, as expected for hydrogen-bonded contacts within *α* helices.

The BS-REDOR fits of $^{13}C\{^{15}N\}$REDOR dephasing of Ala24 $^{13}CH_3$ indicate that 8 ± 2% of the Ala24 methyl carbons are 3.9 ± 0.1 Å from Leu16 amide nitrogen and 8% of Ala24 $^{13}CH_3$ have a $^{13}C-^{15}N$ distance greater than 6 Å (Figure 7C and 7D). The 6 Å distance and its contribution to the 3.9 Å is ill defined due to an experimental limit for maximum REDOR dephasing evolution time of ca. 70 ms. The observed distance of 3.9 Å correlates reasonably well with the corresponding distance (3.5 Å) between helices *A* and *G* in the crystal structure of **GCN4-pAA**, which provides support that the single heptad registry shift is retained within the structure of the **7HSAP1**-derived fibers. Given that the Ala12 ^{13}CO−Leu16 ^{15}N REDOR dephasing constrains 85% of the peptide to be folded into an *α* helix, 1/7th of 85% (i.e., 12%) of the Ala24 side-chain $^{13}CH_3$ should be within 3.9 Å. Together this suggests that a fraction (2−4%) of the 7-helix bundle structures in the **7HSAP1** assemblies is locally disordered. The presence of the 6 Å distance may be related to disorder in the helical sample. However, the observed distance is too short to correspond to other intramolecular or intermolecular interactions within the 7-helix bundles (vide infra). One possible scenario is that the longer distance may result from local disorder at the ends of the fibrillar assemblies of **7HSAP1**. Modeling studies of **7HSAP1** assemblies (vide infra) provide support for this hypothesis in that the Ala24 CH$_3$ to Leu16 amide ^{15}N distance increases at the ends of stacked assemblies and become less defined, especially in comparison to the internal positions of the nanotube fibril (Figure S9, Supporting Information).

Computational Modeling. While the solid-state NMR measurements on the **7HSAP1*** fibrils were consistent with an assembly based on 7-helix bundles with displaced edges, the distance from the $^{13}C\{^{15}N\}$REDOR measurement (3.9 Å) between the 3-^{13}C-Ala(24) on the helix *A* and the ^{15}N-Leu(16) on the helix *G* differed from the corresponding distance (3.5 Å) measured between structurally homologous positions within the crystal structure of **GCN4-pAA**. In order to better understand this discrepancy between the helix−helix contact distances at the displaced edge, an analysis of the 7-helix bundle structure of **GCN4-pAA** was undertaken. Prior analysis of the side-chain packing within this structure was performed using the program SOCKET[46] and were available in CC+, the coiled-coil structural database.[47,48] SOCKET analysis indicated a complex structure in which knob-into-holes packing occurred over an extended hydrophobic interface involving the *a*−*d*−*e*−*g* residues within multiple helices.

The coiled-coil analysis program samCC[49] was modified to determine the structural parameters associated with individual helices within the structure of **GCN4-pAA**. This algorithm was originally developed to detect deviations in the Crick parameters for 4-helix bundle structures through comparison to an idealized tetrameric coiled-coil model displaying canonical knob-into-holes interactions. Similarly, an idealized 7-helix bundle structure based on central residues 4−31 of the **GCN4-pAA** sequence was constructed using the program BeamMotifCC (see Methods).[50] This structural model (2HY6.ideal.pdb) was employed as a benchmark for analysis of the crystal structure of **GCN4-pAA** (see Supporting Information).

Two significant differences were observed between the actual **GCN4-pAA** structure and the reference model calculated based on Crick's equations (Figure S8, Supporting Information).[50,51] The first difference involved the axial displacement between adjacent helices in the bundle, which corresponded to an average value of 1.41 Å. This displacement can be compared to the average axial rise/residue of 1.51 Å that is associated with individual amino acid residues within an α helix. This feature was noted previously in the crystal structure analysis of **GCN4-pAA**[27] and underlies the screw symmetry of the lock-washer structure.

The second structural difference observed for **GCN4-pAA** vis-à-vis the idealized model structure involved deviations of the minor helical phases, ϕ_1, from the ideal Crick angle values for helices *A* and *G*. Axial rotations corresponded to approximately +7° and −7° for helices *A* and *G*, respectively (Figure S9, Supporting Information). Helices *B*−*F* maintained near-ideal Crick angle values for residues in the heptad repeat units. The net result of the Crick angle deviations in the structure of **GCN4-pAA** was an outward rotation of helices *A* and *G* with respect to the other helices in the bundle. This rotation altered the hydrophobic packing at the displaced edge away from classical knobs-into-holes (*a*,*d* layer) packing toward *x*,*da*-layer packing:[49] *a*−*d*−*g* and *a*−*d*−*e* packing for helices *A* and *G*, respectively.

To understand the influence of the Crick angle deviation on the interhelix separation, a simple model structure for **7HSAP1** was constructed that incorporated the Crick parameters of the idealized 7-helix bundle structure in conjunction with the axial translation observed in the crystal structure of **GCN4-pAA**. The structure fitter module of the Crick coiled-coil parametrization (CCCP) program[52,53] was employed to computationally generate Crick parameters for the 7-helix bundles of the actual and ideal **GCN4-pAA** structures from the corresponding protein database files. The structure generator of the CCCP program was then used to create an idealized 7-helix bundle structure in which an axial translation equivalent to a single amino acid occurred between adjacent helices. The Crick parameters of the idealized in-register model were used as input data, with the exception that the $\Delta Z_{\mathrm{offset}}$, i.e., axial displacement, values were derived from **GCN4-pAA**. The resultant structural model was derived from a 7-helix bundle based on a polypeptide consisting of 35 alanine residues that displayed the axial translation and the displaced edge of the **GCN4-pAA** structure (Ala35_7.pdb).

The distances between methyl carbon atoms on chain *A* and amide nitrogen atoms on chain *G* were measured at structurally homologous positions at the displaced edge within this $[(\mathrm{Ala})_{35}]_7$ structural model. The corresponding N-Ala(16)^{G}-3-C-Ala(24)^{A} distance (4.8 Å) within the model structure was significantly longer than the distances of 3.9 and 3.5 Å derived from ^{13}C{^{15}N}REDOR NMR measurements on **7HSAP1*** and the crystal structure of **GCN4-pAA**, respectively. The longer ^{15}N-Leu(16)^{G}-3-^{13}C-Ala(24)^{A} distance of 3.9 Å for **7HSAP1*** may imply a lesser deviation of the Crick angle values from those observed for the corresponding helices in **GCN4-pAA**. Given that the two sequences are not identical, one might expect that subtle structural differences may occur even though the global conformation of the 7-helix bundle is retained.

Molecular modeling with molecular dynamics simulation was employed for analysis of a stacked assembly of five 7-helix bundle structures of **7HSAP1** in the presence of explicit water. A simulation for 1.2 ns indicated convergence to a model structure (7HSAP1_assembly_MD.pdb) in which noncovalent interactions persisted between helical bundles (see Supporting Information). An average distance of 1.6 Å was observed for the gap between successive helical bundles in the center of the stack. Significant differences were observed in the Crick parameters between internal and terminal bundles within the stacked assembly. CCCP analysis of the central helical bundle of the assembly (7HSAP1_centralbundle.pdb) indicated that its Crick parameters compared quite well to those determined for the 7-helix bundle structure of **GCN4-pAA**, including the deviations in the Crick angles for helices *A* and *G* at the displaced edge. In addition, the ^{15}N-Leu(16)^{G}-3-^{13}C-Ala(24)^{A} distance of 3.5 Å for the central 7-helix bundle model matched the corresponding value for the **GCN4-pAA** structure (see Supporting Information). These results suggest that assembly into the nanotube should not cause significant distortion of the 7-helix bundle structure at internal positions within the assembly. However, the ^{13}C{^{15}N} REDOR measurement indicates that some degree of structural distortion must occur, as judged on the basis of the larger ^{15}N-Leu(16)^{G}-3-^{13}C-Ala(24)^{A} distance. A slight rotation of the helices at the displaced edge would result in a change in the Crick angle vis-à-vis the **GCN4-pAA** structure, which would account for the increased helix−helix distance in **7HSAP1** assemblies. This situation may result from formation of lateral interactions between fibrils and/or removal of waters of solvation, either of which could occur during sample preparation for solid-state NMR experiments.

Substrate Binding Assays.

In analogy to **GCN4-pAA**, the 7-helix bundle subunit of **7HSAP1**-derived fibrils should define a central channel with an internal diameter of 7 Å and a length of ca. 50 Å. The diameter of this channel compares in dimension to the internal cavity of γ-cyclodextrin (γ-CD);[54] therefore, the **7HSAP1** assemblies should be able to accommodate substrates of similar size and shape as molecules that form inclusion complexes with γ-CD. The solvatochromic fluorophore PRODAN,[55] 6-propionyl-2-(*N*,*N*-dimethylamino)-naphthalene, was employed as a structural probe in substrate binding assays as it has been shown to bind in a concentration-dependent manner within the internal cavity of γ-CD[56] (Figure 8).

The fluorescent emission spectrum was monitored as a function of **7HSAP1** concentration at a fixed concentration of PRODAN (1 μM in 10 mM MES buffer, pH 6.0). Upon addition of the peptide, the $\lambda_{\max}$ for the PRODAN emission shifted from 520 to 430 nm and gained strongly in intensity. The observed spectroscopic behavior is commensurate with an increase in hydrophobicity in the environment of the

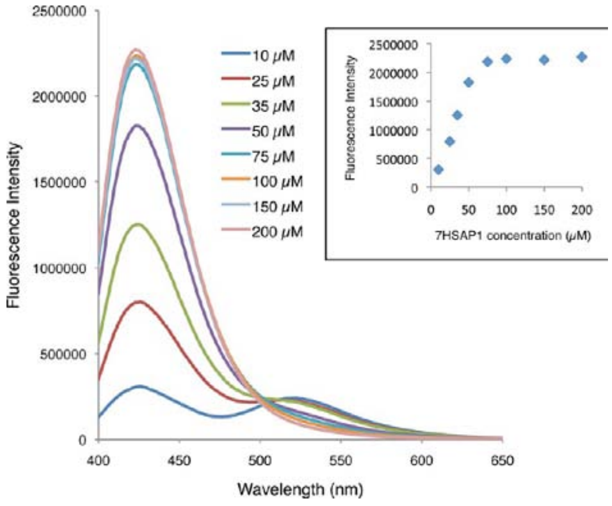

Figure 8. Fluorescence emission spectra from titration of **7HSAP1** into PRODAN (1 μM) in MES buffer (10 mM, pH 6.0). (Inset) Dependence of fluorescence emission intensity at 424 nm on **7HSAP1** concentration.

fluorophore. Similar wavelength displacements have been observed for binding of PRODAN within the hydrophobic internal cavity of γ-CD. In contrast, we performed a similar titration with peptide **YZ1**, which forms a fibrillar structure derived from a coiled-coil dimer.[7a] The fluorescence of PRODAN did not shift in position from the initial λ_{max} value of 520 nm nor did the intensity of the emission increase significantly over the course of the experiment (see Figure S10, Supporting Information). These results suggest that **YZ1** does not bind PRODAN, which supports the hypothesis that PRODAN binds selectively to **7HSAP1** but not generally to coiled-coil assemblies.

In the case of the **7HSAP1**-derived fibrils, the fluorescence data indicate that PRODAN binds within the hydrophobic channel of the 7-helix bundle structures. Fluorescence titration of PRODAN with **GCN4-pAA** under identical conditions afforded a similar spectroscopic response (see Figure S11, Supporting Information), although the binding response did not saturate under the experimental conditions. Since the 7-helix bundle structures of **GCN4-pAA** do not self-associate further under these conditions,[27] the fluorescence response must be associated solely with binding of PRODAN within the central hydrophobic cavity of the **GCN4-pAA** assembly and, by analogy, the 7-helix bundle subunits of the **7HSAP1** nanotubes. We cannot rule out the possibility that PRODAN binding occurs only within bundles that have dissociated from the fibril. However, PRODAN does not affect the global self-assembly of **7HSAP1** as judged from TEM analysis, in which fibrils were observed in the presence of the fluorophore that were identical is structure to those observed in its absence (100 μM **7HSAP1** in the presence of 1 μM PRODAN in 10 mM MES buffer, pH 6.0).

In order to estimate the binding affinity of PRODAN to the **7HSAP1**-derived fibrils, the binding isotherm was determined as a function of peptide concentration (Figure 8, inset). The fluorescence level reached a plateau at a peptide concentration of 75 μM (ca. 10 μM in 7-helix bundle), which is approximately 2 orders of magnitude lower in concentration of the host at ligand saturation than the corresponding values for PRODAN binding to either β- or γ-cyclodextrin.[53] These data confirm that PRODAN binds tightly within the central channel of the **7HSAP1**-derived assemblies. The relatively tight binding response of the peptide-based assembly for PRODAN suggests the potential for encapsulation of shape-appropriate substrates within the nanotube assemblies for controlled release applications.

■ CONCLUSION

Protein-based nanotubes represent attractive candidates for construction of functional nanoporous materials. In native biological systems, tubular structures derived from self-assembly of folded protein domains occur frequently in functional roles that include directional transport,[57] controlled release,[58] and catalysis.[59] Nanotubes derived from native protein assemblies, including tubulin,[60] flagellin,[61] and filamentous viruses,[62] have been explored as structural elements for construction of nanoscale devices for diverse applications.[63,64] However, a far greater repertoire of protein structures is available that display defined internal cavities but do not self-associate to form stable supramolecular assemblies. The functional diversity of nanotube assemblies could be greatly expanded if these nonassembling protein motifs could be recoded at the sequence level to drive self-association into structurally defined assemblies.

This approach has been employed previously with a degree of success to create synthetic protein nanotubes from structurally modified ring-like protein assemblies. Ballister et al.[65] modified the hexameric protein Hcp1 from *Pseudomonas aeruginosa* through introduction of cysteine residues at structurally informed positions at the protein surface. Under oxidizing conditions, the Hcp1 mutant formed nanotubes up to 100 nm in length that consisted of ca. 25 hexameric subunits. Similarly, Miranda et al.[66] introduced cysteine as well as several other mutations at surface positions within the undecameric assembly of TRAP (trp RNA binding attenuation protein) from *Bacillus stearothermophilus*. Surprisingly, the mutant TRAP assembled into nanotubes only in the presence of a bifunctional thiol, which presumably acted indirectly as a cross-linking agent between surface cysteines, albeit at a low level of substitution. Individual nanotubes were observed to be several hundred nanometers in length and could bundle into larger assemblies. This strategy relied mainly on covalent capture through disulfide bond formation to drive nanotube formation, although some degree of surface interaction was implied as a stabilizing influence on nanotube assembly.

In contrast, self-assembly of **7HSAP1** relies exclusively on selective recognition between structurally complementary interfaces to drive self-assembly. These interactions are reinforced through Coulombic attraction between oppositely charged interfaces and, potentially, through hydrogen-bond formation (either directly between peptides or mediated by waters of solvation). Minor alterations introduced into the sequence of **GCN4-pAA** were sufficient to alter its assembly behavior from an isolated heptameric bundle to a nanotube of defined diameter with lengths in the multimicrometer range. Moreover, these high-aspect-ratio assemblies formed at concentrations of **7HSAP1** as low as 100 μM. However, at lower concentrations, the STEM data indicated nanotubes contained imperfections including breaks in continuity and/or the presence of lower mass species. While the structural data are consistent with nanotubes derived from stacking of 7-helix bundles, the interfaces have not been optimized energetically to promote formation of stable contacts.

Tezcan et al. recently reported the stable formation of a complex range of one-, two-, and three-dimensional assemblies, including nanotubes, via metal-mediated self-assembly of cytochrome *cb-562* mutants.[67] The program Rosetta[68] was employed to computationally optimize interactions at the protein−protein interfaces, which enhanced the stability of the resultant assemblies. While the mode of assembly of the cytochrome *cb-562* mutants is different from the lock-washer stacking of **7HSAP1**, computational optimization of the complementary interfaces represents an attractive strategy to further refine formation of nanotube assemblies.

Nonetheless, we demonstrated that simple modification of structurally complementary interfaces within a folded protein structure can drive self-assembly of high-aspect-ratio nanotubes. Moreover, structural analysis across multiple length scales has provided strong supportive evidence that the nanotube assemblies derived from **7HSAP1** comprise subunits that retain the 7-helix bundle of **GCN4-pAA** with minor structural modification. In addition, these nanotubes can bind shape-appropriate small molecules with an affinity that exceeds common host molecules of similar internal dimensions such as cyclodextrins. The external and internal surfaces of the nanotubes are structurally distinct and display the potential for modification through mutagenesis of the peptide sequence. Although the structural plasticity of **7HSAP1** has not been explored, the utility of the corresponding nanotubes would be greatly enhanced if the chemistry of the internal channel could be controlled to facilitate applications in transport and catalysis. Woolfson et al.[37] recently reported that the internal channel of 6-helix bundles was amenable to mutagenesis with retention of the overall fold. While the structure of the 7-helix bundle of **GCN4-pAA** is more complex than the classical knobs-into-holes packing of coiled coils,[47,48] preliminary studies have indicated that the structure is compatible with limited mutagenesis at core residue positions within the peptide sequence.[27] We envision that chemically modified nanotubes derived from **7HSAP1** may offer considerable promise for development of functional nanoporous materials.

■ METHODS

Peptide Synthesis. Peptides **GCN4-pAA** and **7HSAP1** were either purchased from GenScript USA, Inc. (Piscataway, NJ) or synthesized in house. In the latter case, peptides were prepared using microwave-assisted synthesis on a CEM Liberty solid-phase peptide synthesis instrument using a 4-(hydroxymethyl)-phenoxyacetamidomethyl]-PEG-PS resin from Applied Biosystems, Inc. (Foster City, CA). Standard Fmoc protection chemistry was employed with coupling cycles based on HBTU/DIEA-mediated activation protocols and base-induced deprotection (20% piperidine in DMF with 0.1 M HOBt) of the Fmoc group. Peptides were purified via RP-HPLC on a C18 column with a gradient of water−acetonitrile (0.1% trifluoroacetic acid). Purity was assessed to be above 95% by analytical HPLC (Figure S1, Supporting Information). Peptide mass was confirmed using electrospray ionization mass spectrometry (Figure S2, Supporting Information). Peptides were lyophilized, sealed, and stored at −20 °C. Samples for analytical studies were prepared by dissolving the peptide at the appropriate concentration in aqueous MES buffer (10 mM 2-(*N*-morpholino)ethanesulfonic acid, pH 6.0). Peptide solutions were dialyzed against buffer solution to remove the remaining trifluoroacetic acid (MWCO = 2000 Da). The isotopically labeled peptide, 1-^{13}C-Ala(12),^{15}N-Leu(16),3-^{13}C-Ala-(24)-**7HSAP1** (**7HSAP1***), was synthesized, purified, and assembled using an identical procedure. Protected amino acids Fmoc-1-^{13}C-alanine, Fmoc-3-^{13}C-alanine, and Fmoc-^{15}N-leucine were purchased from Cambridge Isotope Laboratories, Inc. (Andover, MA). Labeled amino acids were introduced manually during microwave peptide synthesis. Mass shifts due to incorporation of the labels were confirmed using ESI-mass spectrometry (Figures S1 and S3, Supporting Information).

Circular Dichroism Spectropolarimetry. CD spectra were recorded on a Jasco J-810 CD spectropolarimeter in 0.10 mm quartz cells at a concentration of 100 μM in MES buffer (10 mM, pH 6.0). Spectra were recorded from 260 to 190 nm at a scanning rate of 100 nm/min and a resolution of 0.5 nm. Peptide concentration was determined spectrophotometrically from measurement of the absorbance at 280 nm (A_{280}). For peptides containing Tyr, Trp, or Cys residues, the peptide concentration can be calculated from eq 1

$$\mathrm{MW} \times A_{280}/c = 1280n_{\mathrm{Y}} + 5690n_{\mathrm{W}} + 120n_{\mathrm{C}} \tag{1}$$

in which c is the concentration of peptide in mg/mL and n_{Y}, n_{W}, and n_{C} are the numbers of tyrosine, tryptophan, and cystine residues, respectively, in the peptide sequence.[69] As **7HSAP1** and **GCN4-pAA** and its derivatives contain only a single tyrosine residue per molecule, $c = \mathrm{MW} \times A_{280}/1280$. To eliminate error in determination of absorbance that could arise as a result of UV light scattering due to peptide self-assembly, aqueous solutions of peptide were mixed with 6 M guanidinium chloride in a 1:9 v/v ratio and heated at 100 °C for 15 min to completely denature the sample prior to performing the absorbance measurements.

Flow Linear Dichroism Spectroscopy. Flow linear dichroism spectra were recorded on a JASCO J-810 circular dichroism spectropolarimeter using a microvolume cuvette with a path length of 50 μm and a rotation speed of 3000 rpm to establish Couette flow.[70] Background scattering for each sample was obtained from LD spectra of samples at 0 rpm. LD spectra were measured after 15 min of rotation.

Transmission Electron Microscopy. TEM specimens were prepared from aqueous **7HSAP1** solution in MES buffer (10 mM, pH 6.0). Samples were deposited onto 200 mesh carbon-coated copper grids from Electron Microscopy Sciences (Hatfield, PA). After a 30 s incubation period, excess liquid was wicked away and the specimens were stained with either a 1:1 mixture (v/v) of the negative stains NanoVan (methylamine vanadate, 2%) and Nano-W (methylamine tungstate, 2%) from Nanoprobes, Inc. (Yaphank, NY) or a solution of uranyl acetate (2%). Excess stain was wicked away after incubation on the grid for 1 min. Sample grids were dried under vacuum and stored in a desiccator. TEM measurements were acquired on a Hitachi H-7500 or H-7100 transmission electron microscope at an accelerating voltage of 75 or 100 kV, respectively. Micrographs were recorded at magnifications of 200 000 or 40 000 using a Gatan CCD digital camera.

Cryo-TEM. Aliquots of the protein fiber solution were applied onto glow-discharged, 200 mesh, Quantifoil grids and plunge frozen into liquid ethane using a Mark III Vitrobot (FEI, Hillsboro, OR). Images were collected on a JEOL JEM-2200FS 200 kV field emission transmission electron microscope (JEOL Ltd., Japan) with an in-column Omega energy filter. Images were energy filtered with a slit width of 20 eV. Images were collected under low-dose conditions with the sample maintained at a temperature of circa −177 °C. Images were captured on a high-sensitivity Gatan US4000 4k × 4k Ultrascan CCD camera with minimal defocus applied.

Scanning Transmission Electron Microscopy. STEM data were acquired at Brookhaven National Laboratory (BNL). The STEM instrument operates at 40 keV with a scanning probe of <0.3 nm diameter produced from a cold field emission source. Every electron emerging from the specimen is detected by one of the scintillator-photomultiplier detectors collecting 0−15 (bright field), 15−40 (small-angle dark field), and 40−200 mRadian (large-angle dark field). The large-angle signal is proportional to the mass of atoms in the path of the beam. Specimen quality and mass calibration are checked by detailed comparison of the image to the known structure of tobacco mosaic virus (TMV).

Specimens are deposited on thin carbon (ca. 2 nm thick) supported on a thicker holey carbon film mounted on a titanium grid using the wet-film, hanging-drop method: http://www.bnl.gov/biology/stem/

SpecPrepDetails.asp. TMV is added to the grid first as an internal control, followed by injection buffer, and specimen solution (in 10 mM MES buffer, pH 6.0) for 1 min and then 10 washes of 20 mM ammonium acetate pH 7.0. Excess solution is wicked from the edge with filter paper between each injection. After the last wash the grid is wicked to a thin layer (ca. 1 μm), fast frozen by plunging into liquid nitrogen slush, and stored under liquid nitrogen. Grids are freeze dried overnight in an ion-pumped chamber with an efficient cold trap and transferred under vacuum to the STEM cold stage (−160 °C). Imaging typically uses a dose of 20 el/Å^2 (causing <5% mass loss, corrected by comparison to TMV). Mass measurements are performed off-line with customized software (PCMass, available at ftp.stem.bnl.gov). The program masks out objects significantly above background and computes the value for the thin carbon in the remaining areas, which is subtracted, and pixels within the contour of filaments are summed and divided by length to give mass per unit length. Accuracy is determined by cleanliness of the background between objects and counting statistics of the scattered electrons. At 10 el/Å^2, TMV SD (standard deviation) is ideally ca. 1% and SD of filaments of 6 kDa/nm is ca. 20% for a single segment 10 nm long. For TMV the program provides automatic searching and measurement, but for the thin filaments the low S/N requires manual selection whereupon the software "locks on" to a segment giving angle, offset, and mass per unit length. PCMass also provides statistics in a database for individual images or groups of images.

Solid-State NMR Measurements. The labeled peptide, [1-^{13}C]A12-, [3-^{13}CH$_3$]A24-, [^{15}N]L16-**7HSAP1** (**7HSAP1***), was assembled either in aqueous solution at neutral pH or in the presence of 25 mM MES adjusted to neutral pH. Assembled peptide was pelleted by centrifugation and dried in vacuo. Each NMR sample (25−50 mg) was packed into a 4 mm solid-state NMR rotor and centered using boron nitride spacers. NMR spectra were collected with a Bruker (Billerica, MA) Avance 600 spectrometer using a 4 mm HCN BioSolids magic-angle spinning (MAS) probe. MAS frequency was actively controlled at 10 000 ± 2 Hz with cooling and spinning air exit temperature maintained below −1 °C to ensure MAS and radio-frequency (RF) heating did not denature the samples. ^{13}C (150.8 MHz) CP-MAS spectra before and after REDOR experiments confirmed that the samples did not change during the experiment. The pulse sequence for ^{13}C{^{15}N} rotational-echo double-resonance (REDOR)[44] consists of two parts: an S sequence with both ^{13}C and ^{15}N pulses and the S$_0$ sequence that is identical but does not contain any ^{15}N dephasing pulses. Applying pulses to the dephasing ^{15}N spins interferes with the averaging due to magic-angle spinning and reintroduces the dipolar coupling which is observed in the REDOR S spectrum, where the signal decays according to both T_2 (spin−spin relaxation) and the heteronuclear ^{13}C−^{15}N dipolar coupling. Maximum dephasing occurs when the spacing between π pulses is equal to 1/2 of the rotor period (Tr). The sequence without ^{15}N dephasing π pulses gives the REDOR full-echo or S$_0$ spectra, where magnetization decays according to only T_2. The difference between the REDOR S and the S$_0$ signal (ΔS) is directly proportional to the dipolar coupling and hence the distance between the two spins.

All REDOR data were collected with the ^{13}C of interest placed on-resonance with xy8 ^{13}C{^{15}N}REDOR pulse sequence[71] with dephasing ^{15}N 8 μs π pulses centered at Tr/2 and refocusing ^{13}C 4 μs π pulses centered at Tr and EXORCYCLE phase cycling[72,73] of the final Hahn-echo 4 μs ^{13}C pulse. The xy8 phase cycling compensated for pulse imperfections in both the ^{13}C and the ^{15}N REDOR π pulses. The initial ^{1}H 90° pulse was 1.9 μs, ^{1}H CP RF fields were ramped from 50 to 70 kHz, and the ^{13}C cross-polarization (CP) RF field was kept constant at 50 kHz. A 128 kHz Spinal64 ^{1}H (600.3 MHz) decoupling[74] was applied during REDOR evolution and acquisition. SPINAL64 pulse widths and ^{1}H decoupling resonance frequencies were optimized by comparing the peak heights of the CH and CH$_2$ resonances of fumaric acid monoethyl ester.

The long REDOR evolution times required to measure the weak dipolar couplings between the Ala ^{13}CH$_3$ carbons and the peptide backbone ^{15}Ns are susceptible to RF homogeneity,[73,75] which can lead to a lower REDOR dephasing plateau than predicted with stronger dipolar couplings. Therefore, to determine the proper level for ^{13}C π pulses the power level was arrayed in REDOR S$_0$ pulse sequence at long REDOR evolution times (>50 ms typically corresponding to ca. 500 4 μs ^{13}C π pulses) and choosing the power level that corresponded to the maximum signal intensity.[76] Similarly, ^{15}N 180° pulses were determined by arraying the ^{15}N power level using the REDOR S experiment at REDOR evolution times corresponding to a ΔS/S$_0$ between 0.3 and 0.5.[76]

REDOR data points are the integrated sum of center- and side band peaks. Error bars were calculated using the noise of each spectrum as the maximum peak height deviation. To normalize for the decay due to T_2, individual REDOR curves are plotted as ΔS/S$_0$. The ideal scaling factor was determined with ^{13}C{^{15}N}REDOR spectra of [1-^{13}C,^{15}N]alanine diluted 10:1 with natural abundance alanine. This dilution ratio does not create a perfectly isolated spin pair due to the probability of having an enriched ^{13}C/^{15}N alanine as a next nearest neighbor. Correcting for this, the probe REDOR scaling factor was determined to be 93%. BS-REDOR[45] fits account for the effects of natural abundance ^{13}C contribution to ^{13}CO and ^{13}CH$_3$ REDOR S$_0$ signal and natural abundance ^{15}N dephasing contribution to REDOR S signal intensity.

X-ray Fiber Diffraction and Alignment. Fiber samples were aligned by suspending a droplet of fibril suspension between two wax-tipped glass capillaries (0.7 mm) and air dried at room temperature. Aligned fiber samples were mounted on a goniometer head, and data was collected on a home source Pilatus 6 M detector with a Saturn 944+ CCD. Exposure times were 1−15 s, and the specimen-to-detector distance was 100 mm. Diffraction data were examined using Clearer[43] and X-ray signals measured. Calculated diffraction patterns were generated from input model coordinates (7HSAP1_assembly_MD.pdb or 7HSAP1_centralbundle.pdb) that had first been aligned such the helices ran approximately parallel to the vertical axis of the fiber. Coordinates were placed within a specified unit cell, and calculations were performed using default values[43] with a crystallite size of 400 nm^3 and a sampling size of 1 pixel. Diffraction patterns were compared to experimental data both by visual comparison of the patterns, and radial scans were imported into Microsoft Excel and compared as graphical traces.

Small- and Wide-Angle X-ray Scattering Measurements. Synchrotron SAXS/WAXS measurements were performed at the 12-ID-B beamline of the Advanced Photon Source at Argonne National Laboratory. A SAXS/WAXS simultaneous setup was utilized, and the sample-to-detector distances were set such that the overall scattering momentum transfer q range was achieved from 0.003 to 2.4 Å^{-1}, where $q = 4\pi \sin \theta/\lambda$, 2θ denoting the scattering angle and λ the X-ray wavelength. The wavelength was set at 1.033 Å during the measurements. Scattered X-ray intensities were measured using a Pilatus 2 M (DECTRIS Ltd.) detector for SAXS and Pilatus 300K for WAXS. SAXS/WAXS measurements were performed on aqueous solutions of peptide **7HSAP1** at concentrations of 0.5 or 1 mM in MES buffer (10 mM, pH 6.0) at 25 °C. A flow cell equipped with a quartz capillary (1.5 mm diameter) was used to prevent radiation damage. Twenty images were collected for each sample and buffer. The 2-D scattering images were converted to 1-D SAXS curves through azimuthally averaging after solid angle correction and then normalizing with the intensity of the transmitted X-ray beam using the software package at beamline 12ID-B. The 1-D curves of the samples were averaged and subtracted with the background measured from the corresponding buffers. R_c analysis was done in Igor Pro software (WaveMatrics, Inc.) using the following modified Guinier equation:[41] $\ln[qI(q)] = -R_c^2q^2/2$, where $I(q)$ is the scattering intensity at momentum transfer q. Scattering simulations on hollow cylindrical geometry models were performed in Matlab (MathWorks, Inc.), details described elsewhere.[29d] The scattering simulation on the molecular model (7HSAP1_assembly_MD.pdb) was performed using program CRYSOL.[77] SAXS molecular envelope calculations were performed using program DAMMIN.[42] To reduce the impact of the length heterogeneity and the electron density fluctuation with the molecule, SAXS data with a q range of 0.03−0.56 Å^{-1} was used in the DAMMIN calculations. Due to the intrinsic degeneracy in SAXS data, a tight hollow cylindrical search space with R_{in} of 3, R_{out} of 15, and height of 100 Å was employed for all calculations. Twenty independent individual calculations were performed, and 3-D shape results were further averaged to yield the final envelope.

Fluorescence Spectroscopy. PRODAN (6-propionyl-2-(*N*,*N*-dimethylamino)naphthalene) was purchased from Sigma-Aldrich (St. Louis, MO). Fluorescence spectra were recorded on a Fluoromax-3 spectrophotometer (Horiba Scientific, Inc.) using a quartz cell with a 1 cm path length (Starna Cells, Inc.) at ambient temperature (ca. 22 °C). Emission and excitation slit widths were set to 5 nm. Excitation wavelength was set to 371 nm. Before each measurement, an aliquot (1 μL) of a PRODAN stock solution (1 mM in ethanol) was mixed with 1 mL of peptide solution at the appropriate concentration to obtain a PRODAN concentration of 1 μM. Mixtures were equilibrated at ambient temperature for 6 h before taking fluorescence measurements. Fluorescence spectra were recorded over the wavelength range of 400−650 nm.

Computational Analyses. The programs MSMS[32] and CASTp[31] were employed to analyze the solvent-accessible surface area and internal void volume, respectively, of the 7-helix bundle structure of **GCN4-pAA** (PDB ID 2HY6). The solvent-accessible surface area calculation was performed using MSMS on the NIH server.[78] CASTp calculations were performed using the web-based resource at the University of Illinois, Champaign−Urbana.[79] A modified version of the samCC[46] program was used to quantify the deviation of the **GCN4-pAA** crystal structure from a reference 7-helix bundle. The reference structure was modeled as canonical coiled coil adopting knobs-into-holes packing using the BeamMotifCC program.[50] SamCC not only provided the detailed information on the local variations in **GCN4-pAA** but also allowed generation of an idealized model that is in agreement with the reference structure (2HY6.ideal.pdb; see Supporting Information).

The Crick Coiled-Coil Parameterization (CCCP) program[52] was employed through the web-based server at Dartmouth University.[53] The pdb files for **GCN4-pAA** and its ideal, in-register structure were uploaded into the structure fitter module of CCCP. Residues 4−31 of the corresponding structure of **GCN4-pAA** (PDB ID 2HY6) and the corresponding residues of its idealized counterpart (2HY6.ideal.pdb, see Supporting Information) were fit using this program. Structural parameters generated from analysis of 2HY6.ideal.pdb were loaded into the structure generator of the CCCP program with the exception that ΔZ_{offset} values were derived from the wild-type structure of **GCN4-pAA**. The resulting model (Ala35_7.pdb) consisted of a 7-helix bundle comprising 35-residue peptides based on a polyalanine backbone. The same parameters were employed in CCCP to create a 7-helix bundle structure consisting exclusively of 175-residue (i.e., five repeats of 35 residues) polyalanine sequences. This structure was employed as the input for subsequent molecular modeling studies

Molecular Models. The structural model consisting of the 7-helix bundle polyalanine sequence of 175 residues was split into peptides of 35 residues in length, which were arranged as five separate 7-helix bundles. Side chains were mutated to match the **7HSAP1** sequence, and the resultant 7-helix bundle structure was energy minimized in Macromodel (Schrodinger, Inc.)[80] with 200 steps of steepest decent. The resulting assembly was placed in a simulation box with explicit waters and neutralizing chloride anions. Molecular dynamics simulation was performed for 1.2 ns using the Desmond simulation package[81] and the OPLS-AA/SPC force field.[82] PDB files of the stacked assembly (7HSAP1_assembly_MD.pdb) and the central 7-helix bundle (7HSAP1_centralbundle.pdb) provided models for determination of distance measurements at the displaced edge between helices *A* and *G*, for comparison to REDOR NMR measurements on **7HSAP***, and for simulations of solution SAXS/WAXS measurements and X-ray fiber diffraction data.

■ ASSOCIATED CONTENT

Ⓢ Supporting Information

Additional experimental characterization of peptides and peptide assemblies; structural models of 7-helix bundle assemblies from modeling studies are provided as pdb files. This material is available free of charge via the Internet at http://pubs.acs.org.

■ AUTHOR INFORMATION

Corresponding Author

vcontic@emory.edu

Present Address

$School of Life Sciences, University of Warwick, Coventry CV4 7AL, United Kingdom

Notes

The authors declare no competing financial interest.

■ ACKNOWLEDGMENTS

V.P.C. would like to dedicate this article to Professor David Tirrell on the occasion of his 60th birthday. We thank Stefan Lutz for use of the spectrofluorimeter. Gevorg Grigoryan is acknowledged for advice on the use of the program CCCP. V.P.C. acknowledges financial support from NSF (CHE-1012620) for peptide synthesis and preliminary structural characterization and the Division of Chemical Sciences, Geosciences, and Biosciences, Office of Basic Energy Sciences of the U.S. Department of Energy through Grant (DE-ER15377) for solid-state NMR and electron microscopy. This work was supported in part by Emory University, Children's Healthcare of Atlanta, the Center for AIDS Research at Emory University (P30 AI050409), and the Georgia Research Alliance to E.R.W. and NSF grant 0923395 to E.R.W. This work benefited from the use of the APS funded by the US DOE Office of Basic Energy Sciences, Division of Material Sciences, under contract W-31-109-Eng-38. Electron microscopy was performed with equipment housed in and the support of the Emory University Robert P. Apkarian Integrated Electron Microscopy Core. The circular dichroism spectropolarimeter was obtained from funds derived from NSF grant CHE-0131013.

■ REFERENCES

(1) Loquet, A.; Habenstein, B.; Lange, A. *Acc. Chem. Res.* **2013**, DOI: 10.1021/ar300320p.

(2) Zhou, Z. H. *Adv. Protein Chem. Struct. Biol.* **2011**, *82*, 1−35.

(3) Kojima, S.; Kuriki, Y.; Yoshida, T.; Yazaki, K.; Miura, K. *Proc. Jpn. Acad. Ser. B* **1997**, *73*, 7−11.

(4) (a) Pandya, M. J.; Spooner, G. M.; Sunde, M.; Thorpe, J. R.; Rodger, A.; Woolfson, D. N. *Biochemistry* **2000**, *39*, 8728−34. (b) Ryadnov, M. G.; Woolfson, D. N. *Nat. Mater.* **2003**, *2*, 329−32. (c) Ryadnov, M. G.; Woolfson, D. N. *Angew. Chem., Int. Ed.* **2003**, *42*, 3021−3. (d) Papapostolou, D.; Smith, A. M.; Atkins, E. D.; Oliver, S. J.; Ryadnov, M. G.; Serpell, L. C.; Woolfson, D. N. *Proc. Natl. Acad. Sci. U.S.A.* **2007**, *104*, 10853−8. (e) Sharp, T. H.; Bruning, M.; Mantell, J.; Sessions, R. B.; Thomson, A. R.; Zaccai, N. R.; Brady, R. L.; Verkade, P.; Woolfson, D. N. *Proc. Natl. Acad. Sci. U.S.A.* **2012**, *109*, 13266−71.

(5) Ogihara, N. L.; Ghirlanda, G.; Bryson, J. W.; Gingery, M.; DeGrado, W. F.; Eisenberg, D. *Proc. Natl. Acad. Sci. U.S.A.* **2001**, *98*, 1404−9.

(6) Potekhin, S. A.; Melnik, T. N.; Popov, V.; Lanina, N. F.; Vazina, A. A.; Rigler, P.; Verdini, A. S.; Corradin, G.; Kajava, A. V. *Chem. Biol.* **2001**, *8*, 1025−32.

(7) (a) Zimenkov, Y.; Conticello, V. P.; Guo, L.; Thiyagarajan, P. *Tetrahedron* **2004**, *60*, 7237−46. (b) Zimenkov, Y.; Dublin, S. N.; Ni, R.; Tu, R. S.; Breedveld, V.; Apkarian, R. P.; Conticello, V. P. *J. Am. Chem. Soc.* **2006**, *128*, 6770−1. (c) Dublin, S. N.; Conticello, V. P. *J. Am. Chem. Soc.* **2008**, *130*, 49−51.

(8) Wagner, D. E.; Phillips, C. L.; Ali, W. M.; Nybakken, G. E.; Crawford, E. D.; Schwab, A. D.; Smith, W. F.; Fairman, R. *Proc. Natl. Acad. Sci. U.S.A.* **2005**, *102*, 12656–61.

(9) Dong, H.; Paramonov, S. E.; Hartgerink, J. D. *J. Am. Chem. Soc.* **2008**, *130*, 13691–5.

(10) (a) Aggeli, A.; Bell, M.; Boden, N.; Keen, J. N.; Knowles, P. F.; McLeish, T. C.; Pitkeathly, M.; Radford, S. E. *Nature* **1997**, *386*, 259–62. (b) Aggeli, A.; Nyrkova, I. A.; Bell, M.; Harding, R.; Carrick, L.; McLeish, T. C.; Semenov, A. N.; Boden, N. *Proc. Natl. Acad. Sci. U.S.A.* **2001**, *98*, 11857–11862. (c) Aggeli, A.; Bell, M.; Carrick, L. M.; Fishwick, C. W. G.; Harding, R.; Mawer, P. J.; Radford, S. E.; Strong, A. E.; Boden, N. *J. Am. Chem. Soc.* **2003**, *125*, 9619.

(11) (a) Zhang, S.; Holmes, T.; Lockshin, C.; Rich, A. *Proc. Natl. Acad. Sci. U.S.A.* **1993**, *90*, 3334–8. (b) Marini, D. M.; Hwang, W.; Lauffenburger, D. A.; Zhang, S.; Kamm, R. D. *Nano Lett.* **2002**, *2*, 295–299.

(12) Janek, K.; Behlke, J.; Zipper, J.; Fabian, H.; Georgalis, Y.; Beyermann, M.; Bienert, M.; Krause, E. *Biochemistry* **1999**, *38*, 8246–8252.

(13) Matsumura, S.; Uemura, S.; Mihara, H. *Chem.—Eur. J.* **2004**, *10*, 2789–2794.

(14) Dong, H.; Paramonov, S. E.; Aulisa, L.; Bakota, E. L.; Hartgerink, J. D. *J. Am. Chem. Soc.* **2007**, *129*, 12468–72.

(15) (a) Bowerman, C. J.; Liyanage, W.; Federation, A. J.; Nilsson, B. L. *Biomacromolecules* **2011**, *12*, 2735–45. (b) Swanekamp, R. J.; DiMaio, J. T.; Bowerman, C. J.; Nilsson, B. L. *J. Am. Chem. Soc.* **2012**, *134*, 5556–9.

(16) Choo, D. W.; Schneider, J. P.; Graciani, N. R.; Kelly, J. W. *Macromolecules* **1996**, *29*, 355–366.

(17) (a) Schneider, J. P.; Pochan, D. J.; Ozbas, B.; Rajagopal, K.; Pakstis, L.; Kretsinger, J. *J. Am. Chem. Soc.* **2002**, *124*, 15030–7. (b) Pochan, D. J.; Schneider, J. P.; Kretsinger, J.; Ozbas, B.; Rajagopal, K.; Haines, L. *J. Am. Chem. Soc.* **2003**, *125*, 11802–3. (c) Nagarkar, R. P.; Hule, R. A.; Pochan, D. J.; Schneider, J. P. *J. Am. Chem. Soc.* **2008**, *130*, 4466–74.

(18) O'Leary, L. E.; Fallas, J. A.; Bakota, E. L.; Kang, M. K.; Hartgerink, J. D. *Nat. Chem.* **2011**, *3*, 821–8.

(19) Xu, F.; Li, J.; Jain, V.; Tu, R. S.; Huang, Q.; Nanda, V. *J. Am. Chem. Soc.* **2012**, *134*, 47–50.

(20) Kar, K.; Ibrar, S.; Nanda, V.; Getz, T. M.; Kunapuli, S. P.; Brodsky, B. *Biochemistry* **2009**, *48*, 7959–68.

(21) Rele, S.; Song, Y.; Apkarian, R. P.; Qu, Z.; Conticello, V. P.; Chaikof, E. L. *J. Am. Chem. Soc.* **2007**, *129*, 14780–7.

(22) Przybyla, D. E.; Chmielewski, J. *J. Am. Chem. Soc.* **2008**, *130*, 12610–1.

(23) (a) Cejas, M. A.; Kinney, W. A.; Chen, C.; Leo, G. C.; Tounge, B. A.; Vinter, J. G.; Joshi, P. P.; Maryanoff, B. E. *J. Am. Chem. Soc.* **2007**, *129*, 2202–3. (b) Cejas, M. A.; Kinney, W. A.; Chen, C.; Vinter, J. G.; Almond, H. R., Jr.; Balss, K. M.; Maryanoff, C. A.; Schmidt, U.; Breslav, M.; Mahan, A.; Lacy, E.; Maryanoff, B. E. *Proc. Natl. Acad. Sci. U.S.A.* **2008**, *105*, 8513–8.

(24) (a) Yamazaki, C. M.; Asada, S.; Kitagawa, K.; Koide, T. *Biopolymers* **2008**, *90*, 816–23. (b) Koide, T.; Homma, D. L.; Asada, S.; Kitagawa, K. *Bioorg. Med. Chem. Lett.* **2005**, *15*, 5230–3.

(25) Kotch, F. W.; Raines, R. T. *Proc. Natl. Acad. Sci. U.S.A.* **2006**, *103*, 3028–33.

(26) (a) Bruning, M.; Kreplak, L.; Leopoldseder, S.; Müller, S. A.; Ringler, P.; Duchesne, L.; Fernig, D. G.; Engel, A.; Ucurum-Fotiadis, Z.; Mayans, O. *Nano Lett.* **2010**, *10*, 4533–7. (b) King, N. P.; Sheffler, W.; Sawaya, M. R.; Vollmar, B. S.; Sumida, J. P.; André, I.; Gonen, T.; Yeates, T. O.; Baker, D. *Science* **2012**, *336*, 1171–4. (c) Fletcher, J. M.; Harniman, R. L.; Barnes, F. R.; Boyle, A. L.; Collins, A.; Mantell, J.; Sharp, T. H.; Antognozzi, M.; Booth, P. J.; Linden, N.; Miles, M. J.; Sessions, R. B.; Verkade, P.; Woolfson, D. N. *Science* **2013**, *340*, 595–9.

(27) Liu, J.; Zheng, Q.; Deng, Y.; Cheng, C. S.; Kallenbach, N. R.; Lu, M. *Proc. Natl. Acad. Sci. U.S.A.* **2006**, *103*, 15457–62.

(28) (a) Valery, C.; Artzner, F.; Paternostre, M. *Soft Matter* **2011**, *7*, 9583–94. (b) Bong, D. T.; Clark, T. D.; Granja, J. R.; Ghadiri, M. R. *Angew. Chem., Int. Ed. Engl.* **2001**, *40*, 988–1011.

(29) (a) Ghadiri, M. R.; Granja, J. R.; Milligan, R. A.; McRee, D. E.; Khazanovich, N. *Nature* **1993**, *366*, 324–7. (b) Vauthey, S.; Santoso, S.; Gong, H.; Watson, N.; Zhang, S. *Proc. Natl. Acad. Sci. U.S.A.* **2002**, *99*, 5355–60. (c) Reches, M.; Gazit, E. *Science* **2003**, *300*, 625–7. (d) Lu, K.; Jacob, J.; Thiyagarajan, P.; Conticello, V. P.; Lynn, D. G. *J. Am. Chem. Soc.* **2003**, *125*, 6391–3. (e) Valéry, C.; Paternostre, M.; Robert, B.; Gulik-Krzywicki, T.; Narayanan, T.; Dedieu, J. C.; Keller, G.; Torres, M. L.; Cherif-Cheikh, R.; Calvo, P.; Artzner, F. *Proc. Natl. Acad. Sci. U.S.A.* **2003**, *100*, 10258–62. (f) Morris, K. L.; Zibaee, S.; Chen, L.; Goedert, M.; Sikorski, P.; Serpell, L. C. *Angew. Chem., Int. Ed. Engl.* **2013**, *52*, 2279–83.

(30) O'Shea, E. K.; Klemm, J. D.; Kim, P. S.; Alber, T. A. *Science* **1991**, *254*, 539–544.

(31) Binkowski, T. A.; Naghibzadeh, S.; Liang, J. *Nucleic Acids Res.* **2003**, *31*, 3352–5.

(32) Sanner, M. F.; Olson, A. J.; Spehner, J. C. *Biopolymers* **1996**, *38*, 305–20.

(33) Bennett, M. J.; Sawaya, M. R.; Eisenberg, D. *Structure* **2006**, *14*, 811–24.

(34) Ponstingl, H.; Henrick, K.; Thornton, J. M. *Proteins* **2000**, *41*, 47–57.

(35) (a) Richardson, J. S.; Richardson, D. C. *Proc. Natl. Acad. Sci. U.S.A.* **2002**, *99*, 2754–9. (b) Pedersen, J. S.; Christensen, G.; Otzen, D. E. *J. Mol. Biol.* **2004**, *341*, 575–588. (c) Rousseau, F.; Serrano, L.; Schymkowitz, J. W. *J. Mol. Biol.* **2006**, *355*, 1037–1047. (d) Monsellier, E.; Chiti, F. *EMBO Rep.* **2007**, *8*, 737–742.

(36) (a) Marrington, R.; Seymour, M.; Rodger, A. *Chirality* **2006**, *18*, 680–90. (b) Rodger, A.; Marrington, R.; Geeves, M. A.; Hicks, M.; de Alwis, L.; Halsall, D. J.; Dafforn, T. R. *Phys. Chem. Chem. Phys.* **2006**, *8*, 3161–71.

(37) Bulheller, B. M.; Rodger, A.; Hicks, M. R.; Dafforn, T. R.; Serpell, L. C.; Marshall, K. E.; Bromley, E. H.; King, P. J.; Channon, K. J.; Woolfson, D. N.; Hirst, J. D. *J. Am. Chem. Soc.* **2009**, *131*, 13305–14.

(38) (a) Baxa, U.; Keller, P. W.; Cheng, N.; Wall, J. S.; Steven, A. C. *Mol. Microbiol.* **2011**, *79*, 523–32. (b) Goldsbury, C.; Baxa, U.; Simon, M. N.; Steven, A. C.; Engel, A.; Wall, J. S.; Aebi, U.; Müller, S. A. *J. Struct. Biol.* **2011**, *173*, 1–13. (c) Hodgkinson, J. L.; Horsley, A.; Stabat, D.; Simon, M.; Johnson, S.; da Fonseca, P. C.; Morris, E. P.; Wall, J. S.; Lea, S. M.; Blocker, A. J. *Nat. Struct. Mol. Biol.* **2009**, *16*, 477–85. (d) Sen, A.; Baxa, U.; Simon, M. N.; Wall, J. S.; Sabate, R.; Saupe, S. J.; Steven, A. C. *J. Biol. Chem.* **2007**, *282*, 5545–50. (e) Baxa, U.; Taylor, K. L.; Wall, J. S.; Simon, M. N.; Cheng, N.; Wickner, R. B.; Steven, A. C. *J. Biol. Chem.* **2003**, *278*, 43717–27.

(39) (a) Zaccai, N. R.; Chi, B.; Thomson, A. R.; Boyle, A. L.; Bartlett, G. J.; Bruning, M.; Linden, N.; Sessions, R. B.; Booth, P. J.; Brady, R. L.; Woolfson, D. N. *Nat. Chem. Biol.* **2011**, *7*, 935–41. (b) Burton, A. J.; Thomas, F.; Agnew, C.; Hudson, K. L.; Halford, S. E.; Brady, R. L.; Woolfson, D. N. *J. Am. Chem. Soc.* **2013**, *135*, 12524–7.

(40) Svergun, D. I. *J. Appl. Crystallogr.* **1992**, *25*, 495–503.

(41) Glatter, O.; Kratky, O. *Small Angle X-ray Scattering*; Academic Press Inc.: New York, 1982.

(42) Svergun, D. I. *Biophys. J.* **1999**, *76*, 2879–86.

(43) Makin, O. S.; Sikorski, P.; Serpell, L. C. *Appl. Crystallogr.* **2007**, *40*, 966–72.

(44) Gullion, T.; Schaefer, J. *J. Magn. Reson.* **1989**, *81*, 196–200.

(45) Gehman, J. D.; Separovic, F.; Lu, K.; Mehta, A. K. *J. Phys. Chem. B* **2007**, *111*, 7802–11.

(46) Walshaw, J.; Woolfson, D. N. *J. Mol. Biol.* **2001**, *307*, 1427–50.

(47) Testa, O. D.; Moutevelis, E.; Woolfson, D. N. *Nucleic Acids Res.* **2009**, *37*, D315–22.

(48) http://coiledcoils.chm.bris.ac.uk/ccplus/search/.

(49) Dunin-Horkawicz, S.; Lupas, A. N. *J. Struct. Biol.* **2010**, *170*, 226–35.

(50) Offer, G.; Hicks, M. R.; Woolfson, D. N. *J. Struct. Biol.* **2002**, *137*, 41–53.

(51) (a) Crick, F. H. C. *Acta Crystallogr.* **1953**, *6*, 685−89. (b) Crick, F. H. C. *Acta Crystallogr.* **1953**, *6*, 689−97.

(52) Grigoryan, G.; Degrado, W. F. *J. Mol. Biol.* **2011**, *405*, 1079−100.

(53) http://arteni.cs.dartmouth.edu/cccp/.

(54) (a) Aree, T.; Hoier, H.; Schulz, B.; Reck, G.; Saenger, W. *Carbohydr. Res.* **2000**, *328*, 399−407. (b) Lindner, K.; Saenger, W. *Biochem. Biophys. Res. Commun.* **1980**, *92*, 933−8.

(55) (a) Weber, G.; Farris, F. J. *Biochemistry* **1979**, *18*, 3075−8. (b) Sun, S.; Heitz, M. P.; Perez, S. A.; Colón, L. A.; Bruckenstein, S.; Bright, F. V. *Appl. Spectrosc.* **1997**, *51*, 1316−22.

(56) Crane, N. J.; Mayrhofer, R. C.; Betts, T. A.; Baker, G. A. *J. Chem. Educ.* **2002**, *79*, 1261−3.

(57) Korten, T.; Månsson, A.; Diez, S. *Curr. Opin. Biotechnol.* **2010**, *21*, 477−88.

(58) Tang, J.; Lander, G. C.; Olia, A. S.; Li, R.; Casjens, S.; Prevelige, P., Jr.; Cingolani, G.; Baker, T. S.; Johnson, J. E. *Structure* **2011**, *19*, 496−502.

(59) Shnyrova, A. V.; Bashkirov, P. V.; Akimov, S. A.; Pucadyil, T. J.; Zimmerberg, J.; Schmid, S. L.; Frolov, V. A. *Science* **2013**, *339*, 1433−6.

(60) Dinu, C. Z.; Bale, S. S.; Zhu, G.; Dordick, J. S. *Small* **2009**, *5*, 310−5.

(61) Kumara, M. T.; Srividya, N.; Muralidharan, S.; Tripp, B. C. *Nano Lett.* **2006**, *6*, 2121−9.

(62) Hou, C.; Luo, Q.; Liu, J.; Miao, L.; Zhang, C.; Gao, Y.; Zhang, X.; Xu, J.; Dong, Z.; Liu, J. *ACS Nano* **2012**, *6*, 8692−701.

(63) Lee, B. Y.; Zhang, J.; Zueger, C.; Chung, W. J.; Yoo, S. Y.; Wang, E.; Meyer, J.; Ramesh, R.; Lee, S. W. *Nat. Nanotechnol.* **2012**, *7*, 351−6.

(64) Miller, R. A.; Presley, A. D.; Francis, M. B. *J. Am. Chem. Soc.* **2007**, *129*, 3104−9.

(65) Ballister, E. R.; Lai, A. H.; Zuckermann, R. N.; Cheng, Y.; Mougous, J. D. *Proc. Natl. Acad. Sci. U.S.A.* **2008**, *105*, 3733−8.

(66) Miranda, F. F.; Iwasaki, K.; Akashi, S.; Sumitomo, K.; Kobayashi, M.; Yamashita, I.; Tame, J. R.; Heddle, J. G. *Small* **2009**, *5*, 2077−84.

(67) (a) Salgado, E. N.; Ambroggio, X. I.; Brodin, J. D.; Lewis, R. A.; Kuhlman, B.; Tezcan, F. A. *Proc. Natl. Acad. Sci. U.S.A.* **2010**, *107*, 1827−32. (b) Brodin, J.; Ambroggio, X.; Tang, C.; Parent, K.; Baker, T.; Tezcan, F. A. *Nat. Chem.* **2012**, *4*, 375−382.

(68) Liu, Y.; Kuhlman, B. *Nucleic Acids Res.* **2006**, *34*, W235−8.

(69) Gill, S. C.; von Hippel, P. H. *Anal. Biochem.* **1989**, *182*, 319−26.

(70) Marrington, R.; Dafforn, T. R.; Halsall, D. J.; MacDonald, J. I.; Hicks, M.; Rodger, A. *Analyst* **2005**, *130*, 1608−16.

(71) (a) Gullion, T.; Baker, D. B.; Conradi, M. S. *J. Magn. Reson.* **1990**, *89*, 479−84. (b) Christensen, A. M.; Schaefer, J. *Biochemistry* **1993**, *32*, 2868−73.

(72) Rance, M.; Byrd, R. A. *J. Magn. Reson.* **1983**, *52*, 221−40.

(73) Sinha, N.; Schmidt-Rohr, K.; Hong, M. *J. Magn. Reson.* **2004**, *168*, 358−65.

(74) Fung, B. M.; Khitrin, A. K.; Ermolaev, K. *J. Magn. Reson.* **2000**, *142*, 97−101.

(75) Weldeghiorghis, T. K.; Schaefer, J. *J. Magn. Reson.* **2003**, *165*, 230−6.

(76) Ni, R.; Childers, W. S.; Hardcastle, K. I.; Mehta, A. K.; Lynn, D. G. *Angew. Chem., Int. Ed.* **2012**, *51*, 6635−8.

(77) Svergun, D.; Barberato, C.; Koch, M. H. J. *J. Appl. Crystallogr.* **1995**, *28*, 768−73.

(78) http://helixweb.nih.gov/structbio/basic.html.

(79) http://sts.bioengr.uic.edu/castp/calculation.php.

(80) *MacroModel*, version 9.9; Schrödinger, LLC: New York, 2012.

(81) Bowers, K. J.; Chow, E.; Huageng, X.; Dror, R. O.; Eastwood, M. P.; Gregersen, B. A.; Klepeis, J. L.; Kolossvary, I.; Moraes, M. A.; Sacerdoti, F. D.; Salmon, J. K.; Shan, Y.; Shaw, D. E. Scalable Algorithms for Molecular Dynamics Simulations on Commodity Clusters, *SC 2006 Conference, Proceedings of the ACM/IEEE Conference on Supercomputing SC '06*, Tampa, FL, Nov 11−17, 2006; ACM Press: New York, 2009; Vol. *43*, pp 515−27.

(82) Kaminski, G. A.; Friesner, R. A.; Tirado-Rives, J.; Jorgensen, W. L. *J. Phys. Chem. B* **2001**, *105*, 6474−6487.